Chemical Geology 664 (2024) 122230

Contents lists available at ScienceDirect

Chemical Geology

journal homepage: www.elsevier.com/locate/chemgeo

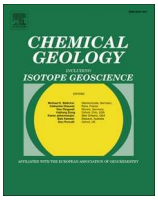

Rare earth elements in the North Atlantic, part I: Non-conservative behavior reveals margin inputs and deep waters scavenging

Marion Lagarde [a,b,*], Viet Quoc Pham [b,c], Pascale Lherminier [d], Moustafa Belhadj [b], Catherine Jeandel [b]

[a] LOCEAN-IPSL, Sorbonne Université/IRD/CNRS/MNHN, Paris, France
[b] LEGOS, CNRS, UT3, CNES, IRD, University of Toulouse, 14 avenue Edouard Belin, Toulouse 31400, France
[c] Institute of Environmental Technology, 18 Hoàng Quốc Việt street, Cầu Giấy, Hanoi, Viet Nam
[d] LOPS, Ifremer, CNRS, IRD, UBO, rue Dumont Durville, Plouzané 29280, France

ARTICLE INFO

Editor: Dr. Karen Johannesson

Keywords:
dREE
Non-conservative behavior
Margin inputs
Iberian margin
Nepheloid layers
Boundary exchange
GEOTRACES
GEOVIDE

ABSTRACT

Dissolved concentrations of 14 Rare Earth Elements (dREE) were measured in seawater samples collected during the GEOVIDE cruise (GEOTRACES GA01, May–June 2014) in the North Atlantic. This is the first dREE dataset produced using the manually operated self-built preconcentration system, made of eight columns of Nobias chelate PA-1® resin (Hitachi High-Technologies) in parallel. Concentration profiles differ from the typical "nutrient-like" dREE vertical distributions. Instead, we observe surface enrichment, especially close to the Iberian margin, and constant or decreasing concentrations below 500 m. An extended Optimum Multiparameter Analysis applied to the GEOVIDE section allowed disentangling the conservative signal brought by water masses from the non-conservative signal produced by inputs or subtractions along the water pathways. Results show i) strong dissolved inputs from the Iberian margin from resuspended particle dissolution, ii) that surprisingly, rather than mixing, scavenging in deep water masses is responsible for the decreasing concentrations at depth, especially in the lower North East Atlantic Deep Water and the Iceland Scotland Overflow Water, and iii) that in the Irminger and Labrador Seas, biological uptake is compensated by external inputs. The combination of lithogenic inputs from the Iberian margin, due to partial dissolution, with scavenging in deep water masses supports that mechanisms occurring at the land-ocean interface explain part of the observations of boundary exchange.

1. Introduction

Trace elements and their isotopes (TEI) play a major role in the ocean biogeochemical cycle (Broecker and Peng, 1982; Bruland and Lohan, 2006; Henderson et al., 2007). Bioactive trace elements, such as iron, manganese, zinc or cobalt, can limit oceanic primary production, and thus the biological pump, the main mechanism for transferring atmospheric carbon to the deep ocean (Martin et al., 1991; Morel and Price, 2003; Boyd et al., 2007). Because eroded crustal materials are significantly more concentrated in bioactive species compared to the ocean, it is essential to quantify and trace this lithogenic source. It is also essential to quantify processes that occur through the water column and cannot be observed directly, such as organic matter remineralization and rates of export, or exchanges between dissolved and particulate phases. These processes regulate the intensity of carbon export to the deep ocean (Broecker and Peng, 1982; Henderson et al., 2007). In other words, quantifying TEI sources, transformation and sink is a major task for marine biogeochemists. To this extent, some trace elements are used as tracers of processes, in which case they are also named proxies. Among these trace elements, the Rare Earth Elements (REE), or lanthanides, are a family of chemical elements ranging in atomic number from 57 (lanthanum) to 71 (lutetium). Products of continental erosion, REE are tracers of lithogenic inputs (Sholkovitz et al., 1999; Tachikawa et al., 1999a; van de Flierdt et al., 2016; Grenier et al., 2018). REE sources to the ocean include rivers, atmospheric inputs (Sholkovitz, 1992; Greaves et al., 1994; Sholkovitz et al., 1999; Tachikawa et al., 1999; Rousseau et al., 2015; Dang et al., 2021; Xu et al., 2023) and inputs from margin and bottom sediment (Haley et al., 2004; Lacan and Jeandel, 2005b; Jeandel et al., 2007; Arsouze et al., 2009; Abbott et al., 2015; Garcia-Solsona and Jeandel, 2020; Deng et al., 2022; Du et al., 2022). However,

* Corresponding author at: LOCEAN-IPSL, Sorbonne Université/IRD/CNRS/MNHN, Paris, France.
E-mail addresses: marion.lagarde@locean.ipsl.fr (M. Lagarde), viet.pham@univ-tlse3.fr (V.Q. Pham), pascale.lherminier@ifremer.fr (P. Lherminier), moustafa.belhadj@univ-tlse3.fr (M. Belhadj), catherine.jeandel@univ-tlse3.fr (C. Jeandel).

https://doi.org/10.1016/j.chemgeo.2024.122230
Received 8 January 2024; Received in revised form 10 June 2024; Accepted 12 June 2024
Available online 16 June 2024

these sources are still insufficiently constrained (Jeandel et al., 1998; Lacan and Jeandel, 2001): as an example, the REE oceanic budget require at least an additional source to be balanced (Tachikawa et al., 2003; Jones et al., 2008; Arsouze et al., 2009).

REE are also informative tracers of dissolved-particle exchange along the water column. Firstly, their atomic mass increases with their atomic number (i.e., along the REE family) while their ionic radius decreases, both resulting from the progressive filling of their 4f orbital. This leads to slightly varying reactivity during geochemical processes from one REE to another. In the ocean, this progressive variation leads to an increase of the proportion of REE complexed with carbonate, phosphate and sulfide ions along the series (Byrne and Kim, 1990; Schijf et al., 2015; Cantrell and Byrne, 1987; Quinn et al., 2006). A higher proportion of light REE (LREE, from lanthanum (La) to gadolinium (Gd); atomic numbers 57–64) is in the form of free cations, making LREE more prone to be exchanged with particles compared to heavy REE (HREE, from terbium (Tb) to lutetium (Lu); atomic numbers 65–71). In other words, the abundance of marine particles as well as their potential adsorption sites, creates a fractionation between LREE and HREE (Sholkovitz et al., 1994; Elderfield, 1988; Elderfield and Greaves, 1982; Tachikawa et al., 1999). The main actors of REE scavenging are manganese oxides and iron hydroxides (Bau et al., 1996; Bau and Koschinsky, 2009; Ohta and Kawabe, 2001), as well as clays (Zhang et al., 2016; Abbott et al., 2019; Andrade et al., 2022) and organic matter (Haley et al., 2004; Hara et al., 2009; Freslon et al., 2014; Sutorius et al., 2022). Among the LREE, cerium (Ce) is even less soluble than its neighbors. In addition to the M^{3+} oxidation state common to all REE, Ce also exists in the M^{4+} oxidation state after adsorption on particles, by biotic or abiotic catalysis (Bau and Dulski, 1996; Elderfield, 1988; Moffett, 1994; Moffett, 1990; Byrne and Kim, 1990). This Ce^{4+} is preferentially removed from solution compared to other REE, which leads to a Ce anomaly: a depletion compared to other REE in the dissolved phase, and a mirror enrichment in the particulate phase. Secondly, the REE reactivity to particles leads to reversible scavenging type profiles in the ocean (Nozaki and Alibo, 2003; Siddall et al., 2008; Garcia-Solsona et al., 2014). A subtraction is observed at the surface where particles are the most abundant, because of REE scavenging by iron hydroxides and manganese oxides (Elderfield, 1988; Byrne and Kim, 1990; Bau and Dulski, 1996). Concentrations then increase with depth, as the particles are dissolved and remineralized, with a concentration gradient more important for LREE than for HREE. Last but not least, REE distributions can also be influenced by biological activity. On the one hand, LREE (mostly lanthanum) can be used by methanotrophs instead of calcium to catalyze methane transformation (Keltjens et al., 2014), leading to their depletion in surface waters (Shiller et al., 2017; Bayon et al., 2020; Meyer et al., 2021). On the other hand, Akagi (2013) suggested that a REE complexation by orthosilicic acid could lead to preferential HREE uptake by the diatoms. To sum up, although LREE and HREE are characterized by similar reactivities in the ocean, they do not display the exact same responses to biogeochemical processes (Oka et al., 2009). For this reason, REE are suitable tracers for describing, understanding and quantifying dissolved-particulate dynamics in the ocean (Sholkovitz et al., 1994; Jeandel et al., 1995; Tachikawa et al., 1999; Kuss et al., 2001).

This study focuses on the behavior of dREE in a key area of the ocean, the subpolar North Atlantic (SPNA, Fig. 1), along the GEOVIDE transect. The GEOVIDE cruise (May–June 2014, R/V Pourquoi Pas?) aimed to provide a basin-scale documentation of trace elements and their isotopes in this area, as part of the GEOTRACES program (Sarthou et al., 2018, www.geotraces.org). The cruise started from Lisbon (Portugal), crossed the western Atlantic basin and the Irminger Sea to reach Cape Farewell, the southern tip of Greenland. The cruise ended in Newfoundland after

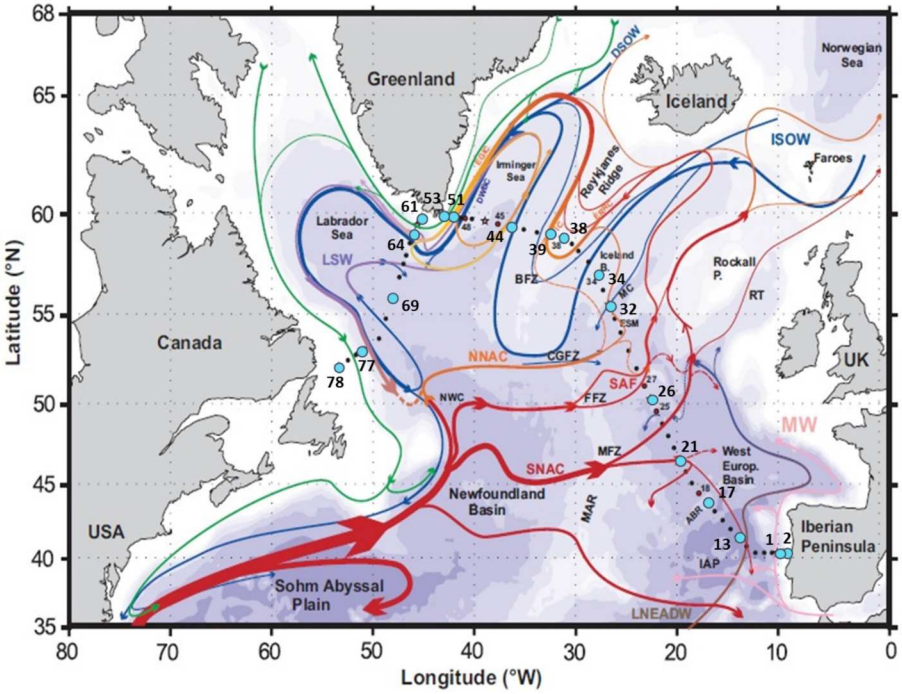

Fig. 1. Map of the studied area (Subpolar North Atlantic, SPNA), including schematized circulation features, adapted from Zunino et al. (2017). Bathymetry color change at 100 m, 1000 m, and every 1000 m below. Fracture zones along the mid-Atlantic Ridge (MAR) are reported: the Bight Fracture Zone, BFZ; the Charles Gibbs Fracture Zone, CGFZ; the Faraday Fracture Zone, FFZ; the Maxwell Fracture Zone, MFZ. Red and green arrows represent the main surface currents; pink and orange arrows represent the currents at intermediate depths; blue and purple arrows represent the deep currents ((N)SNAC: (North) South North Atlantic Current; ERRC: East Reykjanes Ridge Current; IC: Irminger Current; EGIC: East Greenland Irminger Current; DWBC: Deep Western Boundary Current). The main water masses transported by the currents are written with a corresponding color (MW: Mediterranean Water; ISOW: Iceland Scotland Overflow Water; DSOW: Denmark Strait Overflow Water; LSW: Labrador Sea Water; LNEADW: Lower North East Atlantic Deep Water). The small black and large blue dots represent the GEOVIDE section. The blue dots correspond to dREE sampling stations. (For interpretation of the references to color in this figure legend, the reader is referred to the web version of this article.)

crossing the Labrador Sea (Fig. 1). The SPNA is a key area both in the thermohaline circulation, with deep water formation by convection in the Irminger and Labrador Seas (Daniault et al., 2016; Zunino et al., 2017; Mercier et al., 2015), and in terms of primary production with a particularly important spring bloom (Longhurst, 2010; Lemaitre et al., 2018; Fonseca-Batista et al., 2019). The SPNA represents thus a major anthropogenic carbon sink (Khatiwala et al., 2013). Regarding trace elements sources, the studied section is also under the influence of oceanic margins as well as possible atmospheric and hydrothermal inputs.

Particulate REE analysis along the GEOVIDE section revealed that strong lithogenic nepheloids were released from the Iberian margin under the forcing of internal waves and transported offshore by the circulation (Lagarde et al., 2020; Barbot et al., 2022). Estimating the influence of such lithogenic inputs on the composition of the waters flowing along this margin is here of specific interest. In this context, the present study was conducted to answer the following questions: i) to what extent are dREE distributions controlled by water mass mixing? ii) do particulate lithogenic inputs impact dREE concentrations off the margins, and more specifically off the Iberian margin? iii) does the impact of dissolved-particulate exchanges on dREE concentrations vary between biogeochemical provinces?

To do so, seventeen dREE concentration profiles were measured along the GEOVIDE section. The relative contribution of water mass mixing to these concentrations was calculated using an extended Optimum Multiparameter Analysis (eOMPA). The non-conservative dREE fractions deduced from this calculation were then used to discuss particulate-dissolved exchanges and lithogenic inputs within the different biogeochemical regions crossed during the cruise.

2. Material and methods

2.1. Study area: The subpolar North Atlantic

Here, we briefly describe the main water masses along the GEOVIDE transect, as identified by García-Ibáñez et al. (2015, 2018), their

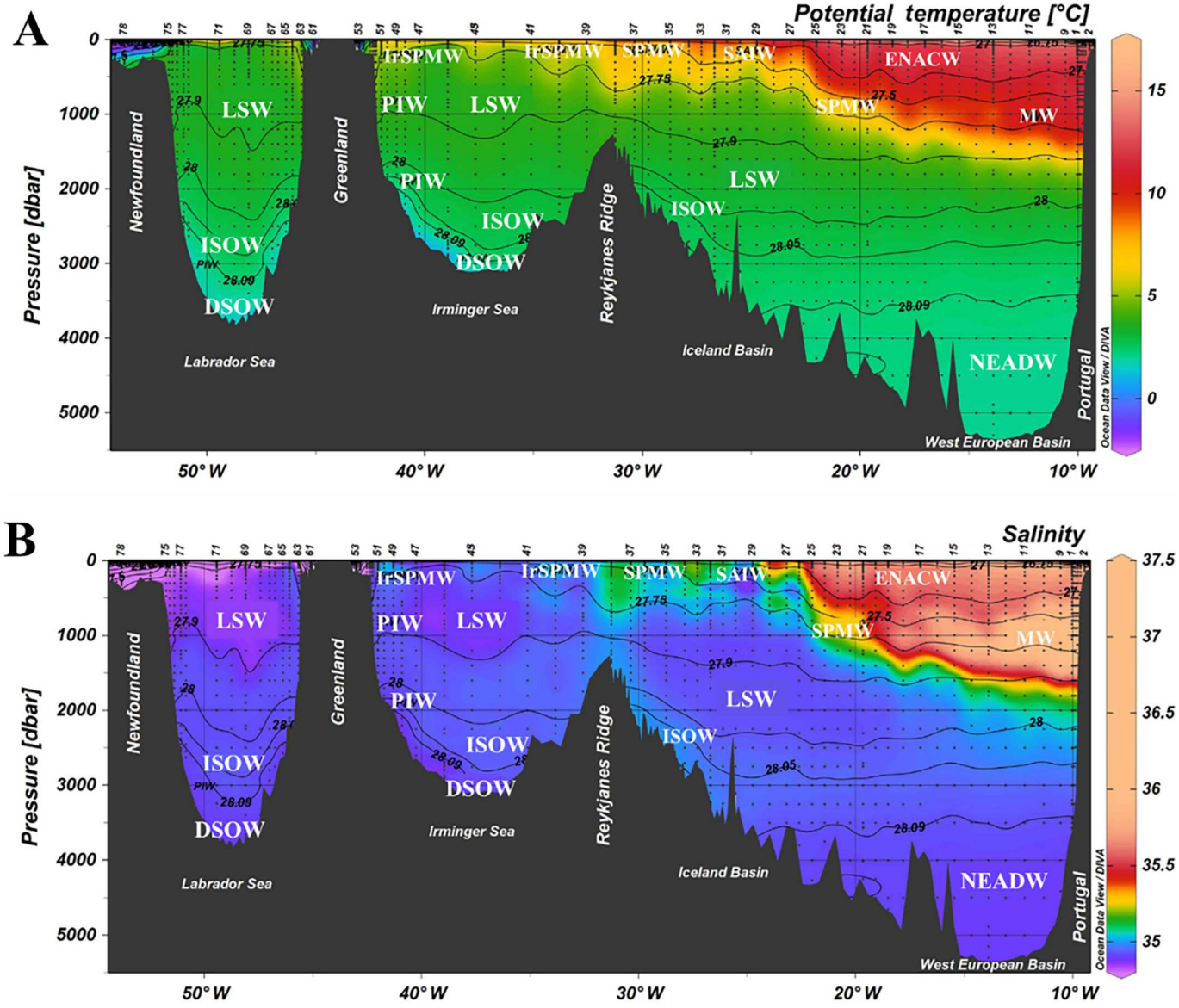

Fig. 2. Adapted from Sarthou et al. (2018). Section plots of A. Potential temperature and B. Salinity along the GEOVIDE transect. Black dots correspond to the data with the numbers on top of each section representing the dREE sampling stations. Water masses are indicated in black: ENACW: East North Atlantic Central Water; MW: Mediterranean Water; NEADW: North East Atlantic Deep Water; SAIW: Subarctic Intermediate Water; IrSPMW: Irminger Subpolar Mode Water; LSW: Labrador Sea Water; ISOW: Iceland Scotland Overflow Water; DSOW: Denmark Strait Overflow Water. Interpolated and plotted with Ocean Data View (Schlitzer, 2023).

circulation and their potential influence on dREE distributions. The study area, the main currents, and the GEOVIDE transect are presented in Fig. 1. The 13 identified water masses are shown on the potential temperature and salinity sections (Fig. 2.A and Fig. 2.B, respectively).

The GEOVIDE section is divided in three areas, characterized by distinct water masses and biogeochemistry: the Iberian margin, the Iceland basin and the Irminger and Labrador Seas (García-Ibáñez et al., 2015, 2018; Lemaitre et al., 2018).

2.1.1. The Iberian margin

This area encompasses stations 1, 2, 13 and 17 (Fig. 1). Here, the North Atlantic current (NAC, in red in Fig. 1) transports the East North Atlantic Central Waters (ENACW, 11.7 °C ≤ θ ≤ 16.6 °C, 35.60 ≤ S ≤ 36.26, Fig. 2) from the subtropics. Below the ENACW, the Mediterranean Water (MW, 1000 m–2000 m, θ = 11.7 ± 0.2 °C, S = 36.50 ± 0.07) is identifiable between 800 m and 1200 m by a maximum of salinity (Fig. 2.B; García-Ibáñez et al., 2015). This area is under the influence of the margin, at the origin of significant inputs of particulate Mn, Fe (Gourain et al., 2019), REE (Lagarde et al., 2020), and in a lesser extend dFe (Tonnard et al., 2018) and dAl (Menzel Barraqueta et al., 2018).

2.1.2. The west European and Iceland basins

This area includes stations 21 and 26 (West European basin), and 32 and 34 (Iceland basin) of the GEOVIDE transect (Fig. 1). It is connected to the Iberian margin by the NAC. The ENACW mixes with the Subpolar Mode Waters (SPMW, 4.4 °C ≤ θ ≤ 8.6 °C, 34.5 ≤ S ≤ 35.29) and the Subarctic Intermediate Water (SAIW, 4.0 °C ≤ θ ≤ 6.5 °C, 34.67 ≤ S ≤ 34.87; García-Ibáñez et al., 2018, García-Ibáñez et al., 2015; Thierry et al., 2008; at 25°W in Fig. 1). This area was the most productive of the transect during the cruise (Fonseca-Batista et al., 2019). The study of particulate REE (pREE, Lagarde et al., 2020) revealed intense exchanges of REE between the dissolved and particulate phases, using pCe anomalies and p(Y/Ho) ratios. Previous studies have shown that both SAIW and SPMW are slightly more concentrated in dREE than the ENACW (Lacan and Jeandel, 2004a, 2004b; Lacan and Jeandel, 2005a, 2005b; Crocket et al., 2018; Shiller, 2021).

2.1.3. The Irminger and Labrador Seas

The Irminger Sea includes stations 38, 44, 51 and 53. The Labrador Sea includes stations 61, 64, 69, 77 and 78 (Fig. 1). Northwest of the Iceland basin, half of the surface waters flows through the main bights in Reykjanes Ridge and circulates into the Irminger Sea (Daniault et al., 2016). Here, at surface and intermediate depths, we find the Irminger Subpolar Mode Water (IrSPMW, 5.02 °C ≤ θ ≤ 5.04 °C, 35.011 ≤ S ≤ 35.027, García-Ibáñez et al., 2015, Fig. 2). Along the Greenland east coast, the IrSPMW is transported by a strong current, the East Greenland Irminger current (EGIC, yellow arrows on Fig. 1). In this area, the IrSPMW mixes with the waters formed along the Greenland slope, the Polar Intermediate Water (θ = 0.0 ± 0.2 °C, S = 34.65 ± 0.03; García-Ibáñez et al., 2015). Filippova et al. (2017) reported dREE enrichment in this water mass resulting from contact with the slope, although particulate distributions did not highlight significant inputs, unlike off the Iberian margin (Lagarde et al., 2020). After Cape Farewell, in the south of Greenland, waters enter the Labrador Sea. This area is mainly occupied by the Labrador Sea Water (LSW, θ = 3.40 ± 0.4 °C, S = 34.86 ± 0.01, García-Ibáñez et al., 2015, Fig. 2), formed by deep convection triggered by air-sea exchanges. This water mass recirculates into the Irminger Sea and the Iceland basin (Fig. 2) at intermediate and deep depths. Filippova et al. (2017) reported relatively constant dREE concentrations in the LSW. The pREE concentrations show lower dissolved-particulate exchanges than in the eastern part of the section (Lagarde et al., 2020). As for the Greenland margin, little influence of the Newfoundland margin was observed by Filippova et al. (2017) and Lagarde et al. (2020). At depth, the bottom of the Irminger and Labrador Seas is occupied by the Denmark Strait Overflow Water (DSOW, θ = 1.30 ± 0.2 °C, S = 34.905 ± 0.01) and the Iceland Scotland Overflow Water (ISOW, θ = 2.7 ± 0.1 °C, S = 35.00 ± 0.02; García-Ibáñez et al., 2018), formed by convection in the Nordic Seas (Daniault et al., 2016; García-Ibáñez et al., 2015, 2018; Zunino et al., 2017). These waters are transported by the Deep Western Boundary Current (DWBC, blue arrow on Fig. 1) along the eastern coast of Greenland, before joining the newly-formed LSW. The water is then exported southward by the DWBC, along the Newfoundland margin (dark blue arrow on Fig. 1). Previous studies have shown that ISOW and DSOW do not present significant dREE enrichment, although their isotopic compositions highlight exchanges with the basalts from Iceland (Filippova et al., 2017) and Norwegian margins (Lacan and Jeandel, 2004a, 2004b; Lacan and Jeandel, 2005a).

2.2. Dissolved REE sampling and analysis

2.2.1. Sampling at sea

Samples were collected using a standard CTD rosette equipped with 24 Niskin bottles. About 10 L of seawater were collected from the Niskin bottles and transferred into 10 L high density polypropylene containers that were rinsed three times with a small amount of sample before being filled. These containers were acid cleaned twice before the cruise, and rinsed three times with Milli-Q water between each sampling. Afterwards, the collected seawater was poured in 30 L Perspex cylinders, with a 0.45 μm Supor filter mounted at the exit. Clean pressurized air was injected at the top of the Perspex cylinders to push seawater through the filters. The Perspex cylinders and the filters were rinsed with ~0.5 L of seawater before the remainder of the sample was poured into the Perspex cylinders. The first 500 mL of the filtered seawater were collected at the exit of the filter into polytetrafluoroethylene bottles. Samples were acidified to pH ~ 2 by addition of HCl, sealed with parafilm and stored into two plastic bags. The remaining volume was dedicated to the analysis of the neodymium isotopic composition. The Perspex cylinders were rinsed with ~1 L of Milli-Q water between each filtration, and acid cleaned halfway through the cruise.

2.2.2. Preconcentration with an offline self-built system

On land, samples were prepared in the LEGOS clean laboratory (Toulouse), by preconcentration and solid phase extraction. Extraction was performed using Nobias-chelate PA-1® resin (Hitachi High-Technology) contained in columns mounted on an offline preconcentration system (Hatje et al., 2014; Pham, 2020, Fig. S1). Briefly, this manifold is composed of 8 handcrafted columns, each column being stacked with two PEEK® valves manually operated. The valve at the top of the column is connected to the reagents used during preconcentration and extraction on one side (Milli-Q water, 0.05 M ammonium acetate buffer, 1 M HNO_3, 0.1 M HCl), and to the sample bottles on the other side. The valve at the exit of the column either lead to the beaker to collect REE or to the waste bottle (Fig. S1, Appendix A). A first peristaltic pump pulls the reagents onto the column, while two other peristaltic pumps each pull four samples onto their respective columns.

The preparation of the samples to be run on the manifold is conducted as follows. Approximately 120 mL of an acidified sample are transferred into a 125 mL low density polyethylene bottle, to which a trispike solution enriched in ^{150}Nd, ^{151}Eu and ^{172}Yb is added. Both sample and spike amounts were weighted precisely. The bottles are then shaken for about 15 h to allow isotopic equilibration. Afterwards, the pH of the samples is adjusted to pH = 4.5 ± 0.2, which after tests is the pH that gives the best REE recoveries after their passage through the Nobias resin (Pham, 2020). The pH adjustment is performed by adding 930 μL of ammonium acetate buffer (NH_4Ac, 7.0 M; pH = 8.0 ± 0.1) and small volumes of 6 M HCl or concentrated NH_4OH, resulting in NH_4Ac concentrations of ~0.05 M in the samples.

The first step of the preconcentration and extraction processes consists in conditioning the columns with ammonium acetate buffer (NH_4Ac, 0.05 M; pH = 4.5 ± 0.2) for 10 min (0.5 $mL.min^{-1}$). This step allows the removal of any acid left, thus ensuring a suitable column pH before loading the sample, and charging the exchange resin sites from

H^+ form to NH_4^+ form (Biller and Bruland, 2012). The samples are then loaded onto the columns at a flow rate of 1 mL.min^{-1}. Later, columns are rinsed with 2 mL of buffer to remove the major cations (e.g., Na^+, K^+, Mg^{2+}, Ca^{2+}) as well as Ba, whose oxides and hydroxides are major sources of interferences in REE measurements. Rare Earth elements are then eluted using 4 mL of 1 M HNO_3, collected in Savillex® vials and evaporated until near-dryness. For each batch, seven samples and one blank were passed through the columns ($n = 34$).

2.2.3. DREE concentration measurement

The measurements were conducted at the Observatoire Midi-Pyrénéees, Toulouse, France, using a sector field-inductively plasma coupled mass spectrometer (SF-ICPMS Element XR; ThermoFisher Scientific®) coupled to an Aridus II^{Tm} (Cetac®) to minimize oxide interferences and increase sensitivity. All REE were measured in low resolution mode and by external calibration. A five-point calibration curve was established at the beginning and the end of each session of analysis to check the linear relationship between measured counts and concentrations. The 50.10^{-12} standard (50 ppt) was measured every six to eight samples. The average between two 50 ppt standards was used to calculate the concentrations of samples ran between these two standards. The calculated concentrations were corrected from oxide and hydroxide interferences. Oxide and hydroxide rates were determined with a mono elemental solution of Ce, by measurement of Ce (isotopes 140 and 142) and the interfered mass (156 and 158 for CeO, and 157 and 159 for CeOH). Other REE and Ba oxide rates were calculated using the constant ratios between REE oxide productions. These ratios were previously determined by measuring REE oxide production rates on the same SF-ICPMS coupled to the Aridus. The ratios between oxide production rates are constant with time (Aries et al., 2000). Oxide contribution was always <0.01% of the signal, thanks to Ba elimination during preconcentration and the use of the Aridus II^{Tm}.

Concentrations of Nd, Eu and Yb were also determined by isotope dilution (ID). Comparison of the ID results to the concentrations calculated using external calibration allowed us to estimate the recovery of the preconcentration procedure. This recovery was then applied to the other REE, following a linear interpolation (Lacan and Jeandel, 2001; Pahnke et al., 2012; Grenier et al., 2013; Garcia-Solsona et al., 2014).

Once corrected from the blank (<0.1 pg.g^{-1}, Fig. S2A, Appendix A), oxide, hydroxide and recovery contributions, the validity of the SF-ICPMS measurement was assessed using the certified reference material (CRM) SLRS-6, run twice at each measurement session. The measured concentrations were within the error bars of the consensus values of Yeghicheyan et al. (2019) obtained by intercalibration between nine laboratories (Fig. S2B, Appendix A). Fifteen GEOVIDE sample concentrations were measured twice during various sessions, and measurement replicates presented a 0%–3% difference.

Because this is the first dataset produced with the aforementioned self-built preconcentration system, its validity was assessed using the CRM SLRS-6, the GEOTRACES SAFe standard and replicates of some of our samples collected for this purpose. SLRS-6, a river water, was passed through each column every few days, while samples ran on the other columns. The SLRS-6 measured concentrations present a 0.2%–10% difference with the average of the consensus values published by Yeghicheyan et al. (2019, Fig. S3A, Appendix A). The SAFe standard, seawater sampled in the Subtropical Northwest Atlantic at 3000 m and widely used in the GEOTRACES program for intercalibrations of trace elements concentrations, was passed through two columns. The measured concentrations lie within the range of valid values published by Behrens et al. (2016) after intercalibration between four laboratories (Table S1 and Fig. S3B, Appendix A, 0.2%–8% of difference depending on the REE). For the GEOVIDE samples, the percentage difference between procedural replicates varies between 0.3% and 8% (Fig. S3C, Appendix A). For La, some values were abnormally low compared to others and to the literature (<20 pmol.kg^{-1}, Lacan and Jeandel, 2005a; Lambelet et al., 2016; Filippova et al., 2017; Shiller, 2021). Recovery problems are suspected, yet SLRS-6 and SAFe values obtained at the same time and recoveries of the standard used for external calibration were consistent. These La data are considered 'bad data' (flag 4 following SeaDataNet measure and qualifier flags), and are marked by a * in Table S2. They will not be discussed. For other REE, data compare well with the literature, and are considered as 'good values'. Finally, the dREE concentrations established during this study have been submitted to the GEOTRACES data base and will be included in the 2025 Intermediate Data Product (IDP2025), except for La.

2.3. Determination of the dREE non-conservative fraction

The dREE non-conservative fraction, or dREE in excess noted REE_{xs}, was determined along the GEOVIDE section by subtracting to the measured concentrations the theoretical conservative dREE fraction. The latter was calculated using García-Ibáñez et al. (2015, 2018) extended optimum multiparameter analysis results (eOMPA). García-Ibáñez et al. (2015, 2018) eOMPA follows the method of Tomczak (1981, 1999) and Tomczak and Large (1989). Briefly, source water types (SWTs) were defined by conservative parameters (temperature and salinity) and quasi-conservative parameters (oxygen, nitrate, phosphate and silicate concentrations), corrected from the uptake and release by phytoplankton. Each SWT is characterized by a unique set of values for the chosen parameters. Any point of the section can be considered as a linear combination of these SWTs; thus, the proportion of each SWT at any point of the section where the parameters are measured can be calculated. The linear combination of the SWT for each parameter, plus the mass conservation equation, results in an overdetermined set of mixing equations, that is resolved using the method of least square residuals (Tomczak, 1981, 1999; Tomczak and Large, 1989). For GEOVIDE, García-Ibáñez et al. (2015, 2018) identified 13 SWTs, reported on the θ-S diagram in Fig. S5 and in Fig. 2. The ENACW, SPMW and SAIW were decomposed into two source waters each with differing temperatures in the eOMPA: $ENACW_{12}$, $ENACW_{16}$, $SPMW_8$, $SPMW_7$, $SAIW_6$, $SAIW_4$ (the subscript corresponds to the temperature of the SWT). Their areas of formation are reported in Fig. S4 (Appendix A). The θ-S diagrams of each station sampled for dREE are shown in Fig. S5. End-members hydrographic features are reported in Fig. S6 (Appendix A).

The dREE conservative fraction was then calculated using the relative abundance of the water masses identified along the section, and their concentration in dREE in their area of formation.

The application of OMPA is entirely dependent on these concentrations (Peters et al., 2018; Lawrence et al., 2022). The calculated non-conservative fraction reflects all the processes occurring during the transport of a defined water mass from the source water location to the section. Thus, depending on the choice of source water location, the interpretation of eOMPA results may vary. To illustrate local inputs of an element to the ocean, for example from a margin or the ocean floor, it is preferable to choose end-members on the section. The more distant the end-members are from the section, the more the non-conservative fraction will derive from a set of processes that are difficult to disentangle from each other. However, by choosing end-members on the section only, it can be difficult to highlight significant differences with water mass mixing alone. The application of eOMPA is therefore a compromise in the choice of end-members between data from the section and those available in the literature around the section, with regard to possible processes in the study area. The dREE concentrations in SWTs were established from the literature. Concentration data for the SWTs were defined in agreement with the hydrographic parameters as defined in the eOMPA. For some water masses, the limited availability of dREE data or the absence of nutrient data led to the selection of points that most closely matched the eOMPA constraints. When several dREE data matched the eOMPA constraints, an average of the values was chosen as the dREE concentration in the SWT. The dREE values chosen in the different SWTs are presented in Table 1, and the corresponding locations and depths are presented in Fig. S4 and Table S3. The comparison

between SWTs hydrographic parameter set and nutrient content set in the eOMPA (García-Ibáñez et al., 2018) with dREE SWT ones is presented in Fig. S6 (Appendix A). In some cases (LSW, Northeast Atlantic Deep Water Low NEADWL, $ENACW_{12}$, $SPMW_7$), the dREE concentrations measured along the GEOVIDE section were considered, as these water masses were not mixed with others at some points of the section (pure end-members). For the SWT NEADWL, two possible end-members were considered: one on the section, one more distant on the GA03 transect. The comparison between those two end-members can be found in the Appendix A, Figs. S7 and S8.

The preformed REE fraction was then subtracted to measured dREE concentrations to calculate REE_{xs}. A positive REE_{xs} highlights inputs along the water mass pathway, while a negative REE_{xs} highlights subtraction. The sources of errors in the REE_{xs} calculation are the uncertainties on the relative contributions of the various SWTs at a given location, on the dREE concentrations estimated in the SWTs, and on the measured dREE concentrations. The method to quantify each of these sources of error is developed in the supplementary material (section 3, Appendix A). The main REE_{XS} profiles discussed thereafter are presented with the associated error bars in Fig. S10 (Appendix A). These errors vary from 0.6 to 3.0 pmol.kg^{-1} for Ce, from 0.7 to 3.7 pmol.kg^{-1} for Nd, and from 0.2 to 0.9 pmol.kg^{-1} for Yb.

3. Results

3.1. DREE concentration distributions

The concentrations of all dissolved REE are compiled in Table S2. The concentration sections of three of them, dissolved Ce (dCe), Nd (dNd) and Yb (dYb), are shown in Fig. 3. Fig. 4 presents selected concentrations profiles representative of the regions crossed during the cruise (Iberian margin and Greenland shelf, West European and Iceland basins, Labrador and Irminger Seas). Dissolved Nd and dYb were selected as representative of the dLREE and dHREE respectively, and because they were also measured by isotopic dilution, which is more precise than external calibration. Dissolved Ce was selected because of its more particle reactive behavior, described in the introduction section (De Baar et al., 1983; Moffett, 1990, 1994; Sholkovitz et al., 1994).

Most of the GEOVIDE profiles (Fig. 4) do not follow the typical "nutrient-like" profiles observed for dREE (except dCe), which generally display low surface concentrations increasing with depth (Garcia-Solsona et al., 2014; Zheng et al., 2016; Zhang et al., 2008; Lambelet et al., 2016; Stichel et al., 2012; Pham et al., 2019; Osborne et al., 2015). Instead, they can be classified in three types of profiles:

a) Profiles with high concentrations are observed in the vicinity of the Iberian margin at stations 1, 2 and 13, and on the Greenland shelf at stations 53 and 61 (Fig. 3. A, B, C and Fig. 4 A). For the Iberian margin, the high concentrations are only observed for LREE. The highest concentrations are found at the surface, dCe and dNd concentrations reaching 33.4 pmol.kg^{-1} and 35.2 pmol.kg^{-1} respectively at station 2 at 70 m. Stations 1 and 13 present a peak at 250 m. They also present high concentrations for all dREE, except dCe, below 3000 m for station 1 and below 4000 m for station 13. On the Greenland shelf, all dREE concentrations are high, with concentrations up to 28 pmol.kg^{-1}, 37 pmol.kg^{-1} and 7 pmol.kg^{-1} for dCe, dNd and dYb respectively. DCe profiles follow the other dREE variations.

b) The second type of profiles show a subsurface maximum, and is observed at most of the stations of the West European Basin, Iceland basin and Irminger Sea and Labrador Sea (stations 26, 32, 38, 51, 44, 69 and 77; Figs. 3 and 4). The depth of the maximum varies between 60 m and 300 m. Below this maximum, dREE concentrations decrease or remain relatively constant with depth. The eastern part of the section (West European Basin and Iceland basin) differs from the Irminger Sea in three ways: maxima are more prominent (about +2 pmol.kg^{-1} in the eastern basins and + 0.8 pmol.kg^{-1} in the western basins), concentrations are lower, and concentrations increase closer to the bottom (Fig. 4). Lambelet et al. (2016) do not observe these subsurface maxima in the Irminger Sea, but in the Labrador Sea (their station 9). Their concentration range for Nd (15.7–18.4 pmol.kg^{-1}) is similar to the one in this study, including the subsurface maxima (16.0–18.8 pmol.kg^{-1}).

c) The last type of profile is found at station 17 and in the Labrador Sea (stations 64, 69 and 77, Figs. 3 and 4.C), with dREE concentrations that tend to decrease with depth (ΔREE varies from 3.5 pmol.kg^{-1} to 2 pmol.kg^{-1}). At these stations, dCe profiles also decrease with depth. Subsurface minima are observed at station 17 at 80 m, and at station 64 at 200 m (Figs. 3 and 4.C). the Labrador Sea profiles are in agreement with the rather constant Nd profiles reported by Filippova et al. (2017), and in the same range of concentrations (15.2–19.7 pmol.kg^{-1} vs 16.0–20.5 in this study).

Apart from these three types of profiles, a few, at least in part, display the typical "nutrient-like" dREE distribution. Station 77 presents a "nutrient-like" profile between the surface and 1000 m (Fig. 4.C), but a decrease in the concentrations is observed below. This is also observed at stations 26 and 32 for HREE only (Fig. 4.B). The only dREE profiles showing the typical surface minimum and enrichment with depth along the whole water column are found at station 21 (in the southern North Atlantic Current), dCe excluded.

Table 1
DREE concentrations in the selected end-members (pmol.kg^{-1}).

pmol/kg	$ENACW_{16}$	$ENACW_{12}$	$SPMW_8$	$SPMW_7$	IrSPMW	LSW	MW	ISOW	NEADWL	DSOW	PIW	$SAIW_6$	$SAIW_4$
La	13.8	16.8	23.7	21.3	24.5	18	21.3	22.4	39.0	25.2	36.3	12.9	26.6
Ce	5.9	4.8	7.1	7.1	7.5	6.3	6.6	12.7	7.3	15.7	18.6	7.1	11.4
Pr	2.5	2.9	4.1	4.1	4.3	4.2	3.8	4.1	8.1	5.0	6.2	3.5	4.3
Nd	12.9	13.9	18.0	18.1	19.1	19.2	16.6	19.2	30.9	23.6	26.0	18.1	19.4
Sm	2.51	2.79	3.44	3.49	3.33	3.80	3.40	3.67	7.49	4.00	5.00	3.33	3.33
Eu	0.68	0.69	0.89	0.93	0.66	0.91	0.91	0.99	1.10	1.32	1.21	0.66	0.66
Gd	3.98	4.30	4.71	5.03	4.46	5.51	4.94	4.90	8.93	5.10	6.21	3.82	4.46
Tb	0.56	0.66	0.68	0.78	0.63	0.87	0.86	0.82	1.27	0.63	0.97	0.63	0.63
Dy	4.78	5.01	5.46	5.96	5.83	6.48	6.21	5.83	8.18	6.13	6.80	4.91	5.52
Ho	1.11	1.29	1.35	1.53	1.52	1.65	1.52	1.45	2.11	1.82	1.65	1.21	1.21
Er	4.15	4.16	4.50	5.05	5.39	5.45	5.04	5.39	8.57	5.39	6.01	4.19	5.39
Tm	0.498	0.591	0.654	0.738	0.595	0.789	0.669	0.714	1.327	0.595	0.870	0.595	0.595
Yb	3.56	3.60	4.31	4.58	4.34	4.91	4.70	4.74	9.45	4.62	5.17	4.05	4.62
Lu	0.490	0.583	0.694	0.782	0.571	0.842	0.763	0.800	1.595	0.571	0.860	0.571	0.571
References	Shiller (2021)	this study	Lacan and Jeandel (2004) Crocket et al. (2008)	this study	Lacan and Jeandel (2005)	this study	Greaves et al. (1991)	Lacan and Jeandel (2004)	Shiller (2021)	Lacan and Jeandel (2005)	Fillipova et al. (2017)	Lacan and Jeandel (2005)	

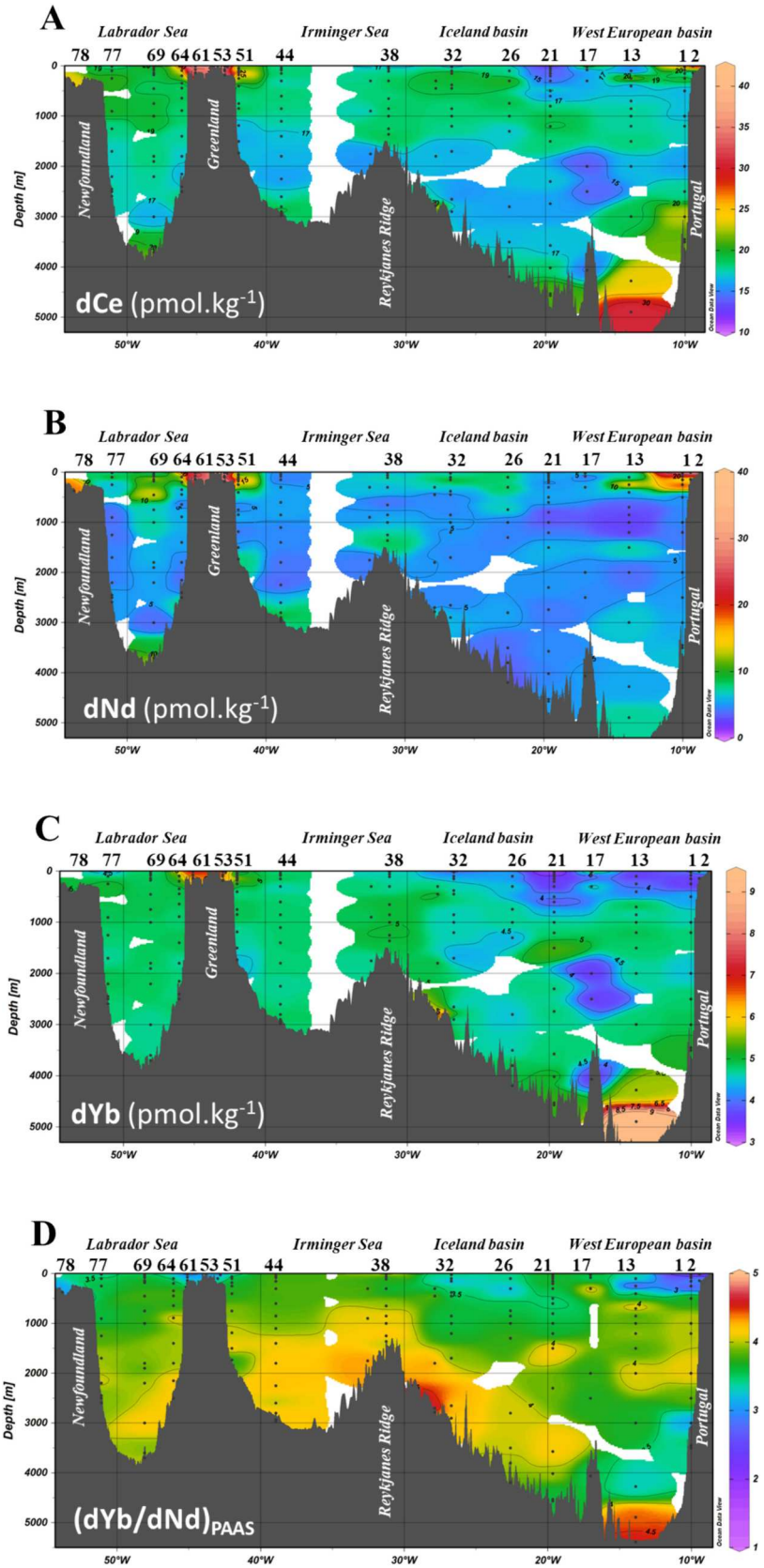

Fig. 3. Concentrations in dissolved A. Ce B. Nd C. Yb and D. (Yb/Nd) ratio normalized to Post- Archean Australian Shale (PAAS) along the GEOVIDE section. Interpolated and plotted with Ocean Data View (Schlitzer, 2023).

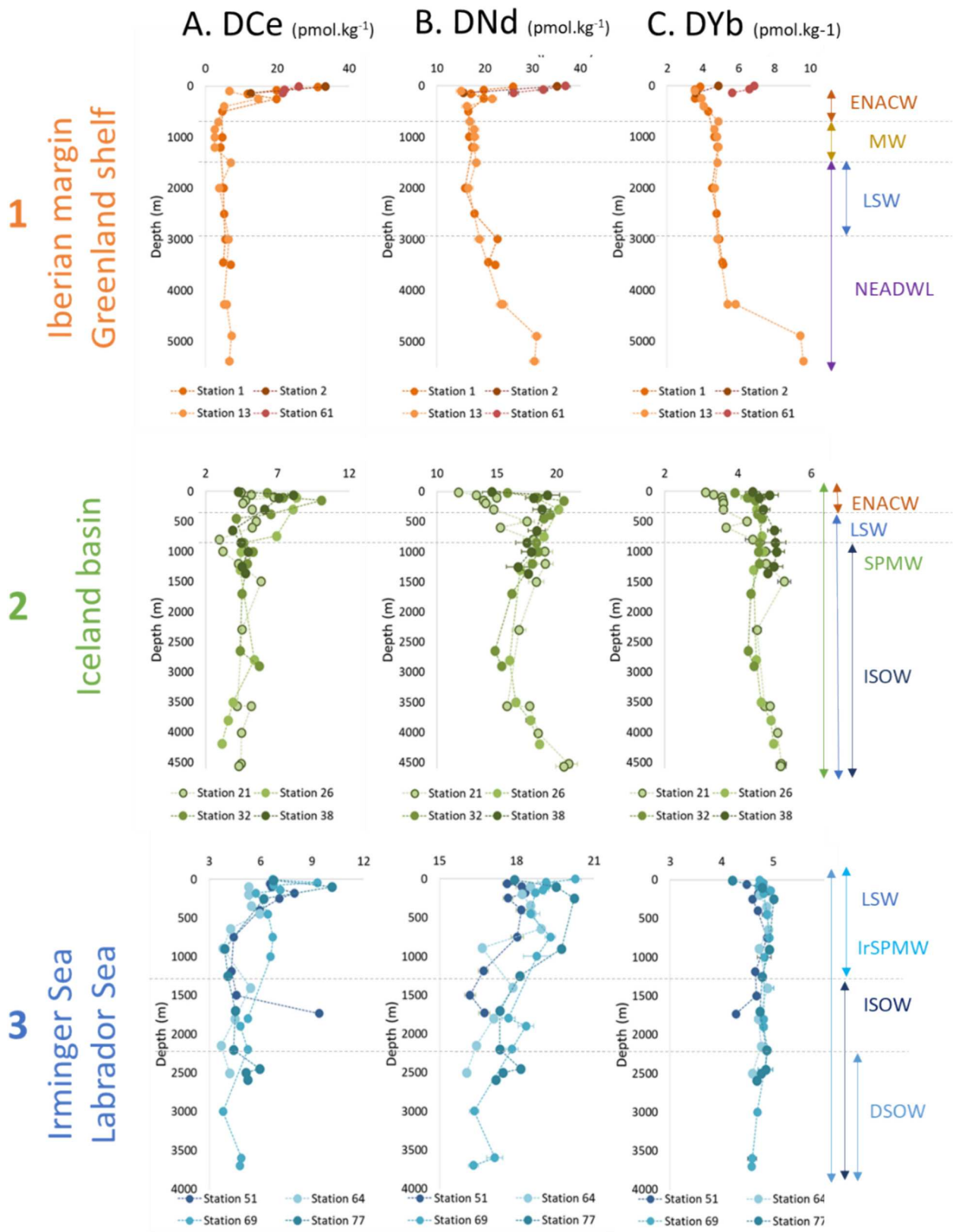

Fig. 4. Dissolved A. Ce, B. Nd, C. Yb concentration profiles at 1. stations 1, 2, 13 and 61 (margin stations, orange and red profiles), 2. at stations 21, 26, 32 and 38 (West European and Iceland Basins, green profiles) and 3. at stations 51, 64, 69 and 77 (Irminger and Labrador Seas, blue profiles). Grey horizontal dotted lines define the main water masses, indicated on the right. Errors bars, representing the 2σ error, are within the point for most of the profiles. (For interpretation of the references to color in this figure legend, the reader is referred to the web version of this article.)

3.2. DREE normalization and patterns

The natural abundance of REE follows a zigzag distribution, with even-numbered elements being more abundant than odd-numbered ones (Oddo-Harkins effect, Harkins, 1917). Therefore, in order to allow identifying and quantifying the fractionation between REE during geochemical processes, their concentrations are normalized to a reference. The reference used in this study is the Post-Australian Archean Shale (PAAS), commonly used for normalizing REE distributions in Earth surface envelopes (critical zone, atmosphere, oceans; Elderfield, 1988). The dREE patterns obtained after normalization to PAAS (Taylor and McLennan, 1985) are presented in Fig. 5. For the sake of clarity, only four stations are represented, the remaining stations displaying similar patterns to one of those four. In addition, concentrations normalized to PAAS were averaged by layers characterized by similar concentrations. Error bars represent the standard deviation associated with these averages. Along the GEOVIDE section, the dREE normalized concentrations show the expected seawater pattern, with enrichment in HREE relative to LREE and depletion in Ce (Fig. 5).

The fractionation between dLREE and dHREE is illustrated by the dYb/dNd ratio normalized to PAAS ($(dYb/dNd)_{PAAS}$, Fig. 5). The dCe depletion relative to other REE was calculated from normalized concentrations, using eq. (1) (Bau and Dulski, 1996; Bolhar et al., 2004):

$$\frac{Ce}{Ce^*} = \frac{[Ce]_{PAAS}}{2*[Pr]_{PAAS} - [Nd]_{PAAS}} \quad (1)$$

The Ce anomaly, Ce/Ce*, is represented by the ratio of the measured Ce concentration and a theoretical concentration calculated following a linear relationship between Nd and Pr concentrations. A ratio $Ce/Ce^* > 1$ means that Ce enrichment is observed in the considered phase compared to other REE. On the opposite, a ratio < 1 indicates a depletion in Ce.

The flattest patterns characterized by the lowest $(dYb/dNd)_{PAAS}$ and closer to 1 Ce/Ce* ratios are observed on the Iberian shelf at station 2 and at the surface of station 1 (Iberian slope) for the 20 m–79 m layer (Fig. 5.A, $(dYb/dNd)_{PAAS} \sim 2$, $0.6 < Ce/Ce^* < 0.9$). The numerical value of the Ce anomaly decreases with depth, where concentrations are low, while the $(dYb/dNd)_{PAAS}$ ratio stays relatively constant. Flattened patterns are also observed at stations 53 and 61 ($(dYb/dNd)_{PAAS} < 3$, $0.36 \leq Ce/Ce^* \leq 0.43$). At other stations, we observe a general decrease in the Ce anomaly numerical value with depth, together with an increase in the $(dYb/dNd)_{PAAS}$ ratio (Fig. 5.C). Those variations are more or less pronounced depending on stations. The progressive depletion in dCe compared to the other dREE is marked at stations 26, 34 and 77 (Fig. 5.B and 5.C). It tends to be constant below a specific depth at stations 17, 32, 38 and 69 (Fig. 5). The patterns at stations 21, 51, 44 and 64 display very few variations (Fig. 5). The lowest $(dYb/dNd)_{PAAS}$ ratios are observed where dYb concentrations are low, i.e. at the surface of stations 26 and 32 ($(dYb/dNd)_{PAAS} < 3.5$) and 1, 2, 53, 54, 61 and 78 ($(dYb/dNd)_{PAAS} < 3$; Fig. 5).

3.3. Non-conservative fractions of dCe, dNd and dYb

The non-conservative fractions of dREE (REE_{XS}) were deduced by subtracting the calculated preformed component from the measured concentrations. A $REE_{XS} > 0$ indicates a local input of dREE, whereas a $REE_{XS} < 0$ indicates a dREE subtraction by scavenging. The results are presented for Ce_{XS}, Nd_{XS} and Yb_{XS} as sections in Fig. 6, as profiles for all dREE in Fig. S9 and as profiles with the associated error for Ce, Nd and Yb in Fig. S10 (Appendix A).

A $REE_{XS} \geq 0$ is generally observed from the surface to ~500 m–1200 m, while a $REE_{XS} < 0$ is observed below. The two points at the bottom of stations 13 and 21 deviate from this trend, presenting a strong dREE enrichment. The highest non-conservative contributions are found from the Iberian margin to the middle of the west European Basin, on the Greenland shelf (station 53 and surface of station 51), and close to the Newfoundland margin (station 77 between the surface and 1000 m). In the west European basin, enrichment is observed between the surface and 1200 m from station 1 to 26. After station 26, where the subpolar front is located, the enrichment is less pronounced and limited to the upper 800 m. In the Irminger and Labrador Seas, REE_{XS} is either slightly negative (for dPr, dNd and dEr) or positive (other dREE), and indicates a strong predominance of water mass mixing over biogeochemical processes.

4. Discussion

Below, the discussion is focused on i) the influence of the primary producers on dREE distribution and fractionation, ii) the intense deep-water scavenging and iii) the influence of the margins surrounding the GEOVIDE section.

4.1. Influence of the primary production at open ocean stations

The West European and Iceland basins were the most productive area encountered during the cruise (Fonseca-Batista et al., 2019; Lemaitre et al., 2018). In this area, high $(Yb/Nd)_{PAAS}$ ratios are observed at the surface of stations 21 (at 15 m, $(Yb/Nd)_{PAAS} = 3.81$) and 38 (at 5 m, $(Yb/Nd)_{PAAS} = 4.36$, Fig. 5). These elevated $(Yb/Nd)_{PAAS}$ ratios suggest a preferential removal of LREE by coccolithophorids. This phytoplanktonic group represented between 45% and 80% of the total chlorophyll-a in surface waters of these basins during the GEOVIDE cruise (Tonnard, 2018; Lemaitre et al., 2018). This is in agreement with the results of Sutorius et al. (2022) incubation experiment, that demonstrated preferential LREE removal during the bloom of an algae that belong to the same class as coccolithophorids.

In the Irminger and Labrador Seas, $(Yb/Nd)_{PAAS}$ ratios are rather homogenously low in the first 500 m and then slightly increase with depth (Fig. 5). In this area, diatoms dominate the phytoplankton communities (Tonnard et al., 2018) and, interestingly, our results support again the preferential scavenging of HREE in the presence of diatoms (Akagi et al., 2011; Akagi, 2013; Lagarde et al., 2020). Nevertheless, our observations differ from those of Sutorius et al. (2022) who observed a preferential LREE scavenging during a diatom bloom generated in a mesocosm experiment.

Correlation coefficients between dREE and nutrients ($Si(OH)_4$ and NO_3 concentrations data from Sarthou et al., 2018) are presented in Fig. 7. Both light (La to Sm) and heavy dREE (Er to Lu) are significantly correlated to $Si(OH)_4$ concentrations (p-value<0.05), although the correlation coefficients are higher for dHREE. In the upper 1500 m, the correlation coefficient increases along the REE series. Below 1500 m to the bottom, correlation coefficients are higher for dLREE than for dHREE, and are significant for La, Pr, Nd, Sm and from Er to Lu. The correlation coefficients with NO_3 are generally lower, but still significant for La, Ce and the heaviest REE (Yb and Lu) considering all the data.

Overall, REE distributions are possibly influenced by biological activity, as suggested by Sutorius et al. (2022) and Haley et al. (2004) who observed REE release in pore water associated to POC degradation, or by Lagarde et al. (2020) who observed sea-water like REE patterns in particles at the surface of the GEOVIDE transect. Recent studies have also established a biological role for methanotrophs (Keltjens et al., 2014; Shiller et al., 2017; Bayon et al., 2020; Meyer et al., 2021), but determining if biological uptake occurs is beyond the scope of this study, especially because of the scarcity of the La data. Regarding all data, dHREE tend to display better correlation with nutrients than LREE, supporting Oka et al. (2009) conclusions about HREE being more influenced by biological processes, when LREE distributions are dominated by sorption processes. The dREE correlation with nutrients is highly variable depending on the depth in the water column. Our results show that correlation coefficients can be similar between LREE and HREE, which may illustrate that the correlation between nutrients and

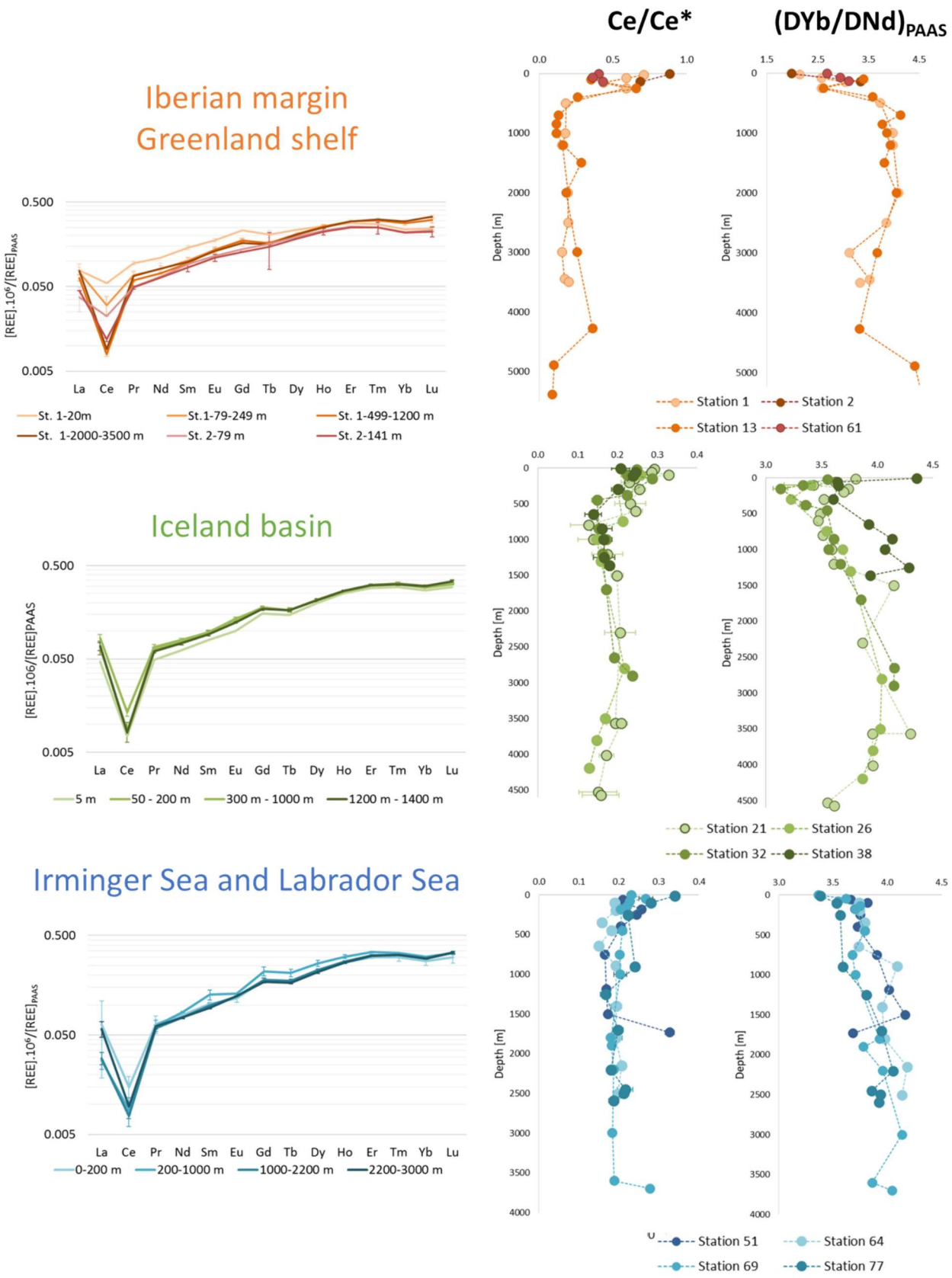

Fig. 5. Left panels: dREE concentrations normalized to PAAS at stations 1 and 2 representative of the Iberian Margin and Greenland shelf (A), station 38 representative of the Iceland basin (B) and station 77 representative of the Irminger and Labrador Seas (C). Concentrations are averaged within layers specified in the legends. Error bars represent the standard deviation associated with the averages. Middle and right panels: Ce/Ce* profiles and dYb/dNd profiles normalized to PAAS at stations 1, 2, 13 and 61 (A; margin stations), at stations 21, 26, 32 and 38 (B; West European and Iceland Basins), and at stations 52, 64, 69 and 77 (C; Irminger and Labrador Seas).

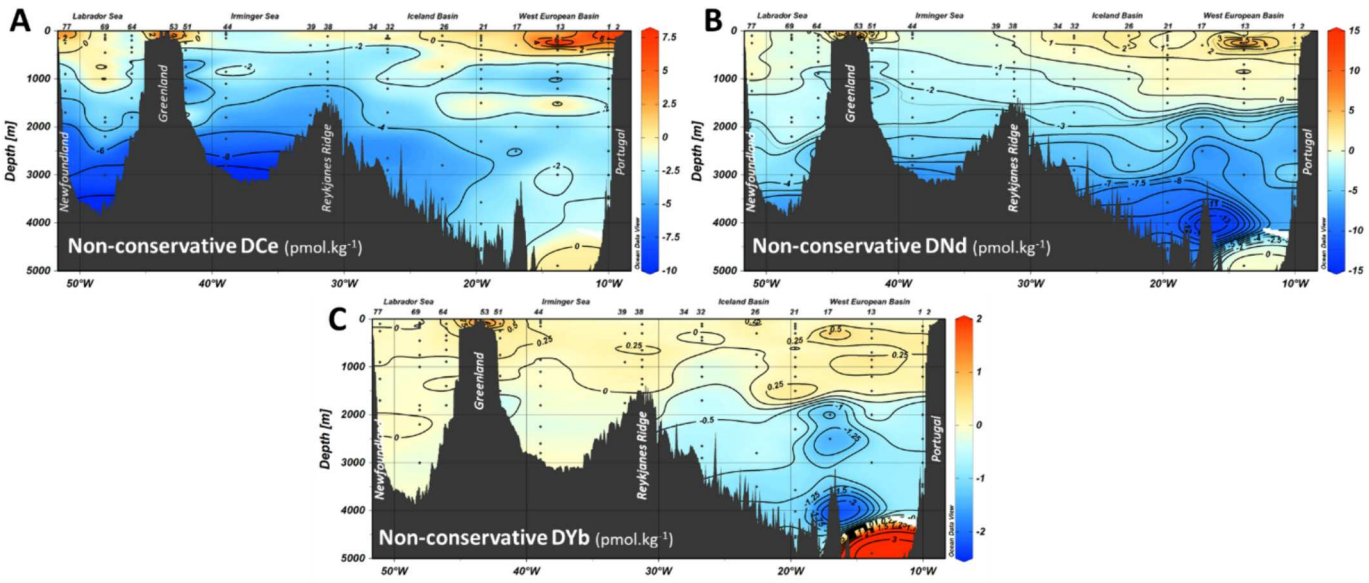

Fig. 6. Section of the non-conservative fractions of dissolved Ce (A), Nd (B) Yb (C) determined using the results of the eOMPA from García-Ibáñez et al. (2018) along the GEOVIDE section. Black dots represent samples to which the eOMPA was applied. The numbers on top of each section are the sampling stations. White color delimited by the "0" contour indicates where concentrations only result from source water types (SWT) mixing and are not influenced by any other source or sink of dREE. Warm orange and blue colors indicate inputs and subtractions of dREE, respectively. Interpolated and plotted with Ocean Data View (Schlitzer, 2023). (For interpretation of the references to color in this figure legend, the reader is referred to the web version of this article.)

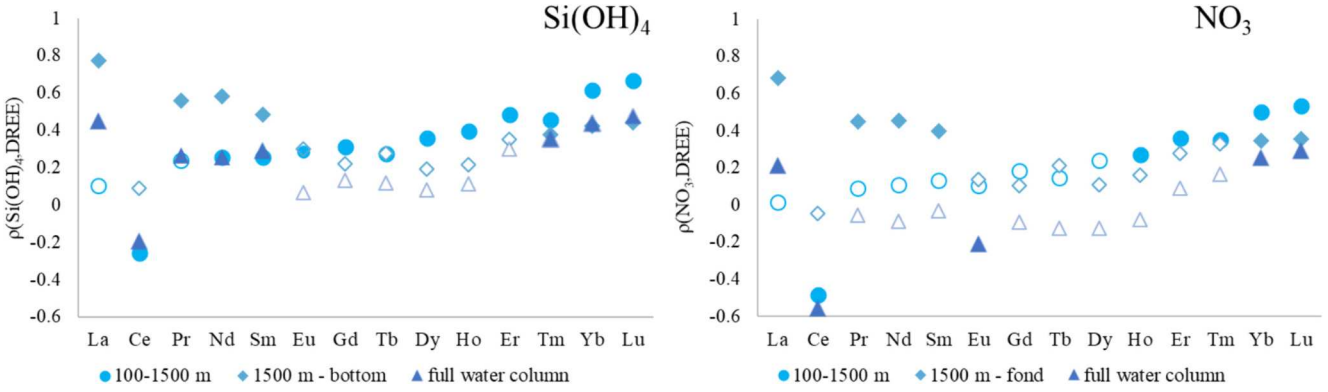

Fig. 7. dREE correlation coefficients with silicates (left panel) and nitrates (right panel) for the whole data set (triangles), from 100 to 1500 m (dots) and from 1500 m to the bottom (diamonds). Solid points correspond to significant correlation coefficients (p-value<0.05), contours to non-significant coefficients (p-value >0.05).

REE results from different processes leading to similar effect on their distributions, e.g., biological uptake and remineralization in one hand, and reversible scavenging in the other hand as proposed by de Baar et al. (2018). These results underline the need for further studies on the influence of different phytoplankton groups on REE distributions, in the dissolved and different particulate phases.

4.2. *Intense scavenging in deep water masses*

In the Irminger Sea, Lambelet et al. (2016) reported dREE profiles remarkably similar to those found in this study (their Fig. 3.A), although with a less pronounced dNd concentration decrease with depth. These results are in agreement with Lacan and Jeandel (2005a) as well. In the Labrador Sea, our results are in good agreement with Filippova et al. (2017) results, who also reported rather homogenous dREE profiles in the Labrador Sea. This area is known for intense convection events that homogenize the upper 2000 m of the water column (Daniault et al., 2016). However, using Nd and Hf isotopic composition, these authors explain the homogenous profiles by similar REE sources in the area (brought through the Denmark Strait by the ISOW and the DSOW), which cannot be discussed with concentrations only in the frame of this study.

Figs. 7 and S9 (Appendix A) show that in deep waters (> 1000 m) dREE are subject to intense scavenging. This subtraction is significant (<0 including error bars, Fig. S10). It should be kept in mind that the quantification of this scavenging depends entirely on the choice of the end-members and SWTs. It demonstrates that the deviation from the typical "nutrient-like" distribution of dREE is not the result from mixing, but from scavenging. The observed subtraction occurs along the entire section for the LREE, and is even affecting the HREE in the west European and Iceland Basins. This subtraction increases with depth and is significant below 1500 m (Fig. S10, Appendix A), despite the relatively large errors. Depletion is more pronounced for Ce and LREE and weakens along the REE series (Fig. 6), according to their solubility. This scavenging is more intense in the east of the section, in the NEADW (stations 13, 21, 26), than in the Irminger and Labrador Seas (Fig. 6). This easternmost area is also characterized by high concentrations in particulate Mn and particles presenting a significant lithogenic fraction, which can generate the observed depletion (Gourain et al., 2019). Subtraction can occur locally or remotely, at the margin, as part of

boundary exchange processes (Lacan and Jeandel, 2005a; Jeandel and Oelkers, 2015; Jeandel, 2016).

In the western part of the section, in the Irminger and Labrador Seas, the concentrations of manganese oxides and iron hydroxides are higher than in the eastern part of the section (Fig. S11, Appendix A), and it is likely that they contribute to the LREE depletion observed in the LSW, ISOW and DSOW. Deng et al. (2018) observed scavenging for Pa and Th in the area, and Chen et al. (2021) associated Pa and Th scavenging to bottom nepheloid layers. The role of Mn oxides and Fe hydroxides in REE scavenging along the GEOVIDE transect is investigated in the Part II of this study (Lagarde et al., 2024).

While scavenging is the main process influencing dREE profiles in the ISOW and DSOW (from 2500 m to the bottom), data show concomitant inputs in the first 1000 m to 1500 m. These inputs display a lithogenic signature, characterized by high Ce/Ce* and $(Yb/Nd)_{PAAS}$ ratios (Fig. 5). This is consistent with the results of Lacan and Jeandel (2004) and Lambelet et al. (2016), who observed a distinct Nd isotope signature in the ISOW in the area, explained by basaltic lithogenic inputs. These results were later confirmed by Le Roy et al. (2018) who applied García-Ibáñez et al. (2018) eOMPA to ^{226}Ra concentrations and who showed positive anomalies in the ISOW of stations 38, 51, 64 and 77. Thus, dREE inputs may find their origin in sediment resuspension followed by particle dissolution, and in their release from pore waters. The latter have been shown to be a major source of REE to the water column (Haley et al., 2005; Abbott et al., 2015, 2019). REE fractionation during this process varies with location in the ocean (Abbott et al., 2015) and it is therefore difficult to conclude about inputs from pore waters in this study without neodymium isotope data. What is clear with our data is that the released REE are then scavenged by the abundant particles of the bottom nepheloid layers.

4.3. Influence of the margins

The $REE_{XS} > 0$ is observed over the entire section for HREE, and at the Iberian margin, in the Iceland basin, on the Greenland shelf and close to the Newfoundland margin for LREE. These enrichments are more pronounced close to the margins (Fig. 6). However, the three margins of the section show differing behaviors: the Iberian margin has a much greater impact on the open ocean than the Greenland and Newfoundland margins.

At the Greenland margin, the signature of the large lithogenic inputs observed on the Greenland shelf (stations 53 and 61; Fig. 3) is not found at the stations on the slope (stations 51 and 64, seawater-type dREE patterns, Fig. 5). These lithogenic inputs remain constrained to the shelf by the East Greenland Irminger Current, as shown by Nd isotopic compositions from Lacan and Jeandel (2004).

Along the Newfoundland margin, slight lithogenic inputs are observed between 2000 m and 3000 m, shown by high Ce/Ce* and $(Yb/Nd)_{PAAS}$ ratios (Fig. 5C). They are consistent with high particulate Fe and Mn concentrations (Gourain et al., 2019) and ^{226}Ra inputs below 1500 m (Le Roy et al., 2018) at stations 77 and 78. These inputs, together with enriched waters from the Baffin Bay and the Hudson Strait, remain constrained to the Labrador current, along the coast, as shown with Nd isotopic composition (Lacan and Jeandel, 2005a; Filippova et al., 2017).

The Iberian margin is characterized by elevated REE_{XS} over the first 1000 m, more pronounced in the first 500 m (Fig. 6; Fig. S9, Appendix A). At stations 1 and 13, above 1200 m, REE_{XS} varies: between 0.1 pmol.kg^{-1} and 7.8 pmol.kg^{-1} for Nd_{XS}, and between 0.14 pmol.kg^{-1} and 0.55 pmol.kg^{-1} for Yb_{XS}. These inputs present a lithogenic imprint, shown by i) flat REE patterns at station 2 and in the upper 250 m layer at station 1, ii) high Ce/Ce* ratios ($Ce/Ce^* \geq 0.4$), showing that the dCe depletion is minor compared to other REE, and iii) low $(Yb/Nd)_{PAAS}$ ratios (Fig. 5A). These characteristics suggest that the inputs are recent, and that Ce oxidation has not fully occurred yet: dLREE have not been preferentially scavenged compared to dHREE. The lithogenic imprint is fading at stations 13 and 17, where the Ce/Ce* ratio decreases, while the $(Yb/Nd)_{PAAS}$ ratio increases. Still, the non-conservative fraction remains significant ($Nd_{XS} > 0$ including the error bars), reflecting that the lithogenic influence is reaching the open ocean (Fig. 6 and S10). The lithogenic source is also supported by the significant lithogenic signature found in the particles at stations 1 and 13 over the first 1000 m (Gourain et al., 2019; Lagarde et al., 2020). The origin of this significant lithogenic input likely comes from the strong activity of internal waves at the Iberian margin, whose energy allows sediment resuspension at various sites (Barbot et al., 2022). Lithogenic particles could then be transported by currents to the GEOVIDE stations (Barbot et al., 2022, Figure S12). Several hypotheses can explain this dissolved REE input displaying a lithogenic imprint: dissolution of the particle lithogenic core, preformed oxide and hydroxide dissolution, or colloidal input from the sediment. It has been shown that lithogenic inputs can occur in the colloid form and be a source of dFe (Homoky et al., 2021). Thus, a colloidal contribution to the dREE enrichment cannot be excluded, but still has to be demonstrated. Between the particle lithogenic core and preformed oxides and hydroxides, we cannot determine exactly which phase dissolves. Looking at the dFe and dMn enrichments along the section could help, as done by Zheng et al. (2016). At some places dFe enrichment is concomitant to dREE one (Tonnard et al., 2018), yet, it is impossible to identify clearly which process dominates between the lithogenic core or the performed oxide and hydroxide dissolution. Likely, in addition to oxides and hydroxides dissolution, part of the lithogenic core dissolves, as it was shown for dusts (Roy-Barman et al., 2021). Overall, these results highlight that a major source of dREE in the east North Atlantic is lithogenic, originating in the sediment of the Iberian margin.

The quantification of the dNd input allows the calculation of the Nd flux from the margin (Eq. 2). Again, this quantification is highly dependent on the eOMPA results which are themselves determined by the choice of end-members. It is therefore an indicative quantity of the importance of this source, which can be compared to other REE sources, as well as with the quantity of sediment brought by the local river Douro.

$$F_{Nd}\left[mol.y^{-1}\right] = \frac{Qv^{*}dNd_{XS}}{D_x} \quad (2)$$

In eq. (2), F_{Nd} is the dissolved Nd flux from the margin at a given depth, established for a year (in mol.y^{-1}); Qv represents the flow rate (calculated in Sv, converted to L.y^{-1}); dNd_{XS} is the non-conservative Nd fraction calculated from the eOMPA (in mol.kg^{-1}), and D_x is the particulate Nd dissolution rate, expressed as a percentage. Qv is calculated using current velocities from Barbot et al. (2022), which range from 1 cm.s^{-1} to 5 cm.s^{-1} between the three resuspension sites at the Iberian margin and the GEOVIDE stations (Barbot et al., 2022, their Fig. 3). The section chosen to calculate the flow is a square of 100 m by 100 m centered on the depth of the observed REE_{XS} positive signal, following Fabre et al. (2019). Arraes-Mescoff et al. (2001) reported dissolution rates ranging from 4% to 14%, for incubation times corresponding to the estimated transport time of the particles. Particle loss by sedimentation was not considered. At the Iberian margin, F_{Nd} varies between 14 and 75 mol.y^{-1} (Fig. 8).

F_{Nd} can be converted into a sediment supply F_{sed} (tons per year), which corresponds to the mass of sediment required to be brought in per year from the margin to reach the Nd_{XS} calculated with the eOMPA (Eq. 3). The Nd concentration in sediment (Nd_{sed}, in µg.g^{-1}) is set to 40 µg.g^{-1} (Nd concentration in the European Shale, representative of the area, Haskin and Haskin, 1966).

$$F_{sed}\left[t.y^{-1}\right] = \frac{F_{Nd}{}^{*}M}{Nd_{sed}} \quad (3)$$

F_{sed} is calculated at station 1 at 200 m and 500 m, and at station 13 at 250 m, in the cores of the nepheloid layers where Nd_{XS} concentrations are available. Fig. 8 summarizes the averaged margin inputs from the various sites of sediment resuspension are summarized in Fig. S12.

Fig. 8 presents the F_{sed} variability as a function of the particle

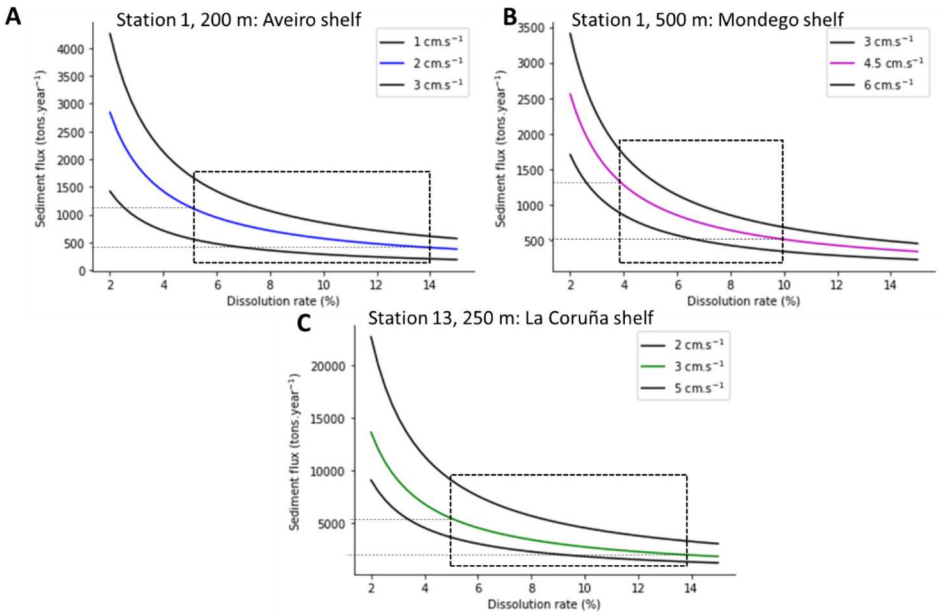

Fig. 8. Sediment flux (in $t.y^{-1}$) at station 1 at 200 m (A) and 500 m (B), and at station 13 at 250 m (C), as a function of the particulate Nd dissolution rates. The black squares define the interval of dissolution rates observed by Arraes-Mescoff et al. (2001) for the predominant current velocities along the pathway, linked to the corresponding sediment fluxes by the black dotted lines.

dissolution rate for the lower, medium and higher current velocities. The lower F_{sed} corresponds to high dissolution rates (14%) and low current velocity (1 $cm.s^{-1}$), and the higher F_{sed} to low dissolution rates (2%) and high current velocities (5 $cm.s^{-1}$). The average F_{Nd} and F_{sed} correspond to a dissolution rate of 6% (Fig. 10). This dissolution rate lies between those established by Arraes-Mescoff et al. (2001) and those obtained from dust incubation by Greaves et al. (1994) and Roy-Barman et al. (2021). The average current velocities were 2 $cm.s^{-1}$ for station 1 at 200 m; 4.5 $cm.s^{-1}$ for station 1 at 500 m, and 3 $cm.s^{-1}$ for station 13 at 250 m (Barbot et al., 2022).

At station 1, F_{sed} is similar at 200 m and 500 m for the two neighbor sites (the Mondego shelf and Aveiro shelf, only 100 km apart, Fig. 8 and S12), with a value of ~900 $t.y^{-1}$ of sediment remobilized at the margin. This consistency supports the computational assumptions, as the current velocities and nepheloid pathways are very different between these two layers (Fig. S12). At Station 13, the flux of sediment stripped from the margin at la Coruña, a more northerly site (Fig. S12; Barbot et al., 2022), is an order of magnitude greater than those at station 1 (Fig. 8).

Although the estimation of the amount of sediment removed from the margin per year is subject to large uncertainties, it is interesting to compare it to the erosion rates available for the Iberian margin in the literature. According to Dias et al. (2002), 96% of the sediment discharged by the Douro river is available for resuspension. This means that $1.2.10^7$ $t.y^{-1}$ of sediment is not retained between 65 m and 130 m (Dias et al., 2002) and can be transported at greater depth or to the open ocean. This amount is 10,000 greater than the calculated sediment flux required here, which makes it compatible as a source for the observed lithogenic inputs, even considering particle loss, dilution or lower dissolution rates.

Overall, our study highlights the importance of margins undergoing significant internal tidal wave energy dissipation as significant sources of dREE in addition to pREE, as well as likely other elements of lithogenic nature such as Fe. This has been observed by Pham et al. (2019, Solomon Sea), Gourain et al. (2019, Iberian margin), Zheng et al. (2016, Angola margin), Lam et al. (2020, Peru margin). Such conjunction between internal dynamic, sediment resuspension and partial dissolution are probably part of the processes contributing to boundary exchange. Indeed, boundary exchange refers to processes occurring at margins that impact the Nd isotopic composition (ε_{Nd}) without significantly modifying Nd concentrations, highlighting unaccounted sources and sinks in Nd oceanic mass balance (Lacan and Jeandel, 2001; Tachikawa et al., 2003; Du et al., 2022). Boundary exchange is well documented for various margins (Lacan and Jeandel, 2001, 2005a; Tachikawa et al., 2003; Carter et al., 2012; Wilson et al., 2012; Grenier et al., 2013; Garcia-Solsona et al., 2014; Basak et al., 2015; Lambelet et al., 2016), and could be partly explained by a combination of particle dissolution and concomitant scavenging, as observed here for the Iberian margin and as suggested by Arsouze et al. (2007), Tachikawa et al. (2003), Lacan and Jeandel (2004a, 2004b) and Jeandel et al. (2013).

5. Conclusion

This study proposes the first dREE dataset acquired with the house-made offline method, that use the Nobias-chelate PA-1® resin (Hitachi High-Technology). This system allows the preconcentration of eight seawater samples simultaneously. This procedure is faster than preconcentration by coprecipitation with iron, produces lower blanks, and is inexpensive.

Using an eOMPA (García-Ibáñez et al., 2018), dREE distributions were separated between a conservative signal, due to water mass mixing, and a non-conservative one, due to local biogeochemical processes. Our results evidence that:

- all along the section, the unusual dREE profiles characterized by a concentration decrease with depth, result from intense scavenging in deep waters by Mn-rich particles, Mn oxides being known REE scavengers.

- the eastern basin is strongly impacted by lithogenic inputs from the Iberian margin, while in the western basin the signal is more homogenous due to the presence of the LSW.

- lithogenic inputs from the Iberian margin lead to significant dREE enrichment by particle dissolution. This highlights the importance of the sedimentary source in the REE (but also other elements such as Fe) cycle. The Iberian margin inputs result from sediment resuspension, triggered by internal tides energy dissipation along the slope. As internal tides are permanent and ubiquitous in the ocean, they are likely at the origin of underestimated sediment inputs to the global ocean, and may thus be at the origin of significant lithogenic trace metals inputs to the ocean. Such process could partly explain the Boundary Exchange mechanism.

- in the western basin, the presence of diatoms raises HREE affinity for particles. HREE are then likely released at depth when opal dissolves, although, the dominant signal observed here is due to scavenging along the whole water column. Mn oxides and Fe hydroxides are likely involved in the scavenging process. This is confirmed in the part II of this study (Lagarde et al., 2024), that investigates the REE affinity for the different particulate fractions. The results show that along the GEOVIDE transect, Mn oxide proportions and in a lesser extent Fe hydroxide proportions are the main drivers of REE scavenging by particles.

Financial support

This research has been supported by the French National Research Agency (grant ANR-13-BS06-0014, ANR-12-PDOC-0025-01), the French National Centre for Scientific Research (grant CNRS-LEFE-CYBER), the LabexMER (grant ANR-10-LABX-19), and Ifremer. It was supported in the logistics by DT-INSU and GENAVIR. The International GEOTRACES Programme is possible in part thanks to the support from the U.S. National Science Foundation (Grant OCE-2140395) to the Scientific Committee on Oceanic Research (SCOR).

CRediT authorship contribution statement

Marion Lagarde: Writing – original draft, Validation, Methodology, Investigation. **Viet Quoc Pham:** Writing – review & editing, Validation, Methodology. **Pascale Lherminier:** Writing – review & editing, Supervision, Project administration, Investigation, Funding acquisition. **Moustafa Belhadj:** Validation, Methodology, Investigation. **Catherine Jeandel:** Writing – review & editing, Validation, Supervision, Project administration, Methodology, Investigation, Funding acquisition, Data curation, Conceptualization.

Declaration of Competing Interest

The authors declare that they have no known competing financial interests or personal relationships that could have appeared to influence the work reported in this paper.

Data availability

All data are included in the supplement

Acknowledgements

We are thankful to the captain, Gilles Ferrand, and crew of the R/V Pourquoi Pas? for their help during the GEOVIDE mission. Geraldine Sarthou, PI of GEOVIDE with Pascale Lherminier (co-author), is acknowledged for her serene management of this long cruise. We would like to give special thanks to Pierre Branellec, Floriane Desprez de Gésincourt, Michel Hamon, Catherine Kermabon, Philippe Le Bot, Stéphane Leizour, Olivier Ménage, Fabien Pérault, and Emmanuel de Saint Léger for their technical expertise and to Catherine Schmechtig for the GEOVIDE database management. We also thank the trace metal clean sampling team.

We thank Aurelie Marquet, Camille Duquenoy, and Jerome Chmeleff for making the (sometimes capricious) HR-ICP-MS operational. We thank Nolwenn Lemaitre for her very careful proofreading of the manuscript. We thank Erika Sternberg for her copy-editing work on the manuscript. We are thankful to the two anonymous reviewers for their constructive comments, which greatly helped to improve the manuscript.

Appendix A. Supplementary data

Supplementary data to this article can be found online at https://doi.org/10.1016/j.chemgeo.2024.122230.

Appendix B. Supplementary data

The supplementary material is composed of four parts:

1. A presentation of the home-made offline preconcentration system, the manifold
2. The dREE concentrations along the GEOVIDE section
3. Details on the eOMPA application, with source water type characteristics, dREE concentrations in these source water types, and selected dREE non-conservative profiles with associated errors.
4. Manganese oxide and iron hydroxide concentrations.

References

Abbott, A.N., Haley, B.A., McManus, J., Reimers, C.E., 2015. The sedimentary flux of dissolved rare earth elements to the ocean. Geochim. Cosmochim. Acta 154, 186–200.

Abbott, A.N., Löhr, S., Trethewy, M., 2019. Are clay minerals the primary control on the oceanic rare earth element budget? Front. Mar. Sci. 6, 504.

Akagi, T., 2013. Rare earth element (REE)–silicic acid complexes in seawater to explain the incorporation of REEs in opal and the "leftover" REEs in surface water: New interpretation of dissolved REE distribution profiles. Geochim. Cosmochim. Acta 113, 174–192.

Akagi, T., Fu, F., Hongo, Y., Takahashi, K., 2011. Composition of rare earth elements in settling particles collected in the highly productive North Pacific Ocean and Bering Sea: implications for siliceous-matter dissolution kinetics and formation of two REE-enriched phases. Geochim. Cosmochim. Acta 75, 4857–4876.

Andrade, G.R.P., Cuadros, J., Barbosa, J.M.P., Vidal-Torrado, P., 2022. Clay minerals control rare earth elements (REE) fractionation in Brazilian mangrove soils. CATENA 209, 105855.

Aries, S., Valladon, M., Polvé, M., Dupré, B., 2000. A Routine Method for Oxide and Hydroxide Interference Corrections in ICP-MS Chemical Analysis of Environmental and Geological Samples. Geostand. Geoanal. Res. 24, 19–31. https://doi.org/10.1111/j.1751-908X.2000.tb00583.x.

Arraes-Mescoff, R., Roy-Barman, M., Coppola, L., Souhaut, M., Tachikawa, K., Jeandel, C., Sempéré, R., Yoro, C., 2001. The behavior of Al, Mn, Ba, Sr, REE and Th isotopes during in vitro degradation of large marine particles. Mar. Chem. 73, 1–19.

Arsouze, T., Dutay, J.-C., Lacan, F., Jeandel, C., 2007. Modeling the neodymium isotopic composition with a global ocean circulation model. Chem. Geol. 239, 165–177.

Arsouze, T., Dutay, J.-C., Lacan, F., Jeandel, C., 2009. Reconstructing the Nd oceanic cycle using a coupled dynamical – biogeochemical model. Biogeosciences 6, 2829–2846.

Barbot, S., Lagarde, M., Lyard, F., Marsaleix, P., Lherminier, P., Jeandel, C., 2022. Internal tides responsible for lithogenic inputs along the iberian continental slope. J. Geophys. Res. Oceans 127 e2022JC018816.

Basak, C., Pahnke, K., Frank, M., Lamy, F., Gersonde, R., 2015. Neodymium isotopic characterization of Ross Sea Bottom Water and its advection through the southern South Pacific. Earth Planet. Sci. Lett. 419, 211–221.

Bau, M., Dulski, P., 1996. Distribution of yttrium and rare-earth elements in the Penge and Kuruman iron-formations, Transvaal Supergroup, South Africa. Precambrian Res. 79, 37–55.

Bau, M., Koschinsky, A., 2009. Oxidative scavenging of cerium on hydrous Fe oxide: Evidence from the distribution of rare earth elements and yttrium between Fe oxides and Mn oxides in hydrogenetic ferromanganese crusts. Geochem. J. 43, 37–47. https://doi.org/10.2343/geochemj.1.0005.

Bau, M., Koschinsky, A., Dulski, P., Hein, J.R., 1996. Comparison of the partitioning behaviours of yttrium, rare earth elements, and titanium between hydrogenetic marine ferromanganese crusts and seawater. Geochim. Cosmochim. Ac. 60, 1709–1725.

Bayon, G., Lemaitre, N., Barrat, J.-A., Wang, X., Feng, D., Duperron, S., 2020. Microbial utilization of rare earth elements at cold seeps related to aerobic methane oxidation. Chem. Geol. 555, 119832.

Behrens, M.K., Muratli, J., Pradoux, C., Wu, Y., Böning, P., Brumsack, H.-J., Goldstein, S. L., Haley, B., Jeandel, C., Paffrath, R., Pena, L.D., Schnetger, B., Pahnke, K., 2016. Rapid and precise analysis of rare earth elements in small volumes of seawater - Method and intercomparison. Mar. Chem. 186, 110–120. https://doi.org/10.1016/j.marchem.2016.08.006.

Biller, D.V., Bruland, K.W., 2012. Analysis of Mn, Fe, Co, Ni, Cu, Zn, Cd, and Pb in seawater using the Nobias-chelate PA1 resin and magnetic sector inductively coupled plasma mass spectrometry (ICP-MS). Mar. Chem. 130–131, 12–20. https://doi.org/10.1016/j.marchem.2011.12.001.

Bolhar, R., Kamber, B.S., Moorbath, S., Fedo, C.M., Whitehouse, M.J., 2004. Characterisation of early Archaean chemical sediments by trace element signatures. Earth Planet. Sci. Lett. 222, 43–60.

Boyd, P.W., Jickells, T., Law, C.S., Blain, S., Boyle, E.A., Buesseler, K.O., Coale, K.H., Cullen, J.J., Baar, H.J.W., Follows, M., Harvey, M., Lancelot, C., Levasseur, M., Owens, N.P.J., Pollard, R., Rivkin, R.B., Sarmiento, J., Schoemann, V., Smetacek, V., Takeda, S., Tsuda, A., Turner, S., Watson, A.J., 2007. Mesoscale iron enrichment experiments 1993-2005: synthesis and future directions. Science 315, 612–617.

Broecker, W.S., Peng, T., 1982. Tracers in the Sea. Eldigio Press Palisades, N.Y, 690 pp.

Bruland, K.W., Lohan, M.C., 2006. 6.02 controls of trace metals in seawater. In: Elderfield, H. (Ed.), Treatise on Geochemistry. Elsevier, 625 pp.
Byrne, R.H., Kim, K.-H., 1990. Rare earth element scavenging in seawater. Geochim. Cosmochim. Acta 54, 2645–2656.
Cantrell, K.J., Byrne, R.H., 1987. Rare earth element complexation by carbonate and oxalate ions. Geochim. Cosmochim. Acta 51, 597–605. https://doi.org/10.1016/0016-7037(87)90072-.
Carter, P., Vance, D., Hillenbrand, C.D., Smith, J.A., Shoosmith, D.R., 2012. The neodymium isotopic composition of waters masses in the eastern Pacific sector of the Southern Ocean. Geochim. Cosmochim. Acta 79, 41–59.
Chen, S.-Y.S., Marchal, O., Lerner, P.E., McCorkle, D.C., Rutgers van der Loeff, M.M., 2021. On the cycling of 231Pa and 230Th in benthic nepheloid layers. Deep Sea Res. Part Oceanogr. Res. Pap. 177, 103627.
Crocket, K.C., Hill, E., Abell, R.E., Johnson, C., Gary, S.F., Brand, T., Hathorne, E.C., 2018. Rare earth element distribution in the NE Atlantic: evidence for benthic sources, longevity of the seawater signal, and biogeochemical cycling. Front. Mar. Sci. 5, 147.
Dang, D.H., Zhang, Z., Wang, W., Oursel, B., Juillot, F., Dupouy, C., Lemonnier, H., Mounier, S., 2021. Tropical mangrove forests as a source of dissolved rare earth elements and yttrium to the ocean. Chem. Geol. 576, 120278.
Daniault, N., Mercier, H., Lherminier, P., Sarafanov, A., Falina, A., Zunino, P., Pérez, F.F., Ríos, A.F., Ferron, B., Huck, T., Thierry, V., Gladyshev, S., 2016. The northern North Atlantic Ocean mean circulation in the early 21st century. Prog. Oceanogr. 146, 142–158.
De Baar, H.J.W., Bacon, M.P., Brewer, P.G., 1983. Rare-earth distributions with a positive Ce anomaly in the Western North Atlantic Ocean. Nature 301, 324–327.
de Baar, H.J.W., Bruland, K.W., Schijf, J., van Heuven, S.M.A.C., Behrens, M.K., 2018. Low cerium among the dissolved rare earth elements in the central North Pacific Ocean. Geochim. Cosmochim. Acta 236, 5–40.
Deng, F., Henderson, G.M., Castrillejo, M., Perez, F.F., 2018. Evolution of 231Pa and 230Th in overflow waters of the North Atlantic. Biogeosci. Discuss. 1–24.
Deng, K., Yang, S., Du, J., Lian, E., Vance, D., 2022. Dominance of benthic flux of REEs on continental shelves: implications for oceanic budgets. Geochem. Perspect. Lett. 22, 26–30.
Dias, J.M.A., Jouanneau, J.M., Gonzalez, R., Araújo, M.F., Drago, T., Garcia, C., Oliveira, A., Rodrigues, A., Vitorino, J., Weber, O., 2002. Present day sedimentary processes on the northern Iberian shelf. Prog. Oceanogr. 52, 249–259. https://doi.org/10.1016/S0079-6611(02)00009-5.
Du, J., Haley, B.A., Mix, A.C., Abbott, A.N., McManus, J., Vance, D., 2022. Reactive-transport modeling of neodymium and its radiogenic isotope in deep-sea sediments: the roles of authigenesis, marine silicate weathering and reverse weathering. Earth Planet. Sci. Lett. 596, 117792.
Elderfield, H., 1988. The oceanic chemistry of the rare-earth elements. *Philos. Trans. R. Soc. Lond.* A 105–126.
Elderfield, H., Greaves, M.J., 1982. The rare earth elements in seawater. Nature 296, 214–219. https://doi.org/10.1038/296214a0.
Fabre, S., Jeandel, C., Zambardi, T., Roustan, M., Almar, R., 2019. An overlooked silica source of the modern oceans: are sandy beaches the key? Front. Earth Sci. 7, 231.
Filippova, A., Frank, M., Kienast, M., Rickli, J., Hathorne, E., Yashayaev, I.M., Pahnke, K., 2017. Water mass circulation and weathering inputs in the Labrador Sea based on coupled Hf–Nd isotope compositions and rare earth element distributions. Geochim. Cosmochim. Acta 199, 164–184.
Fonseca-Batista, D., Li, X., Riou, V., Michotey, V., Deman, F., Fripiat, F., Guasco, S., Brion, N., Lemaitre, N., Tonnard, M., Gallinari, M., Planquette, H., Planchon, F., Sarthou, G., Elskens, M., LaRoche, J., Chou, L., Dehairs, F., 2019. Evidence of high N2 fixation rates in the temperate Northeast Atlantic. Biogeosciences 16, 999–1017.
Freslon, N., Bayon, G., Toucanne, S., Bermell, S., Bollinger, C., Chéron, S., Etoubleau, J., Germain, Y., Khripounoff, A., Ponzevera, E., Rouget, M.-L., 2014. Rare earth elements and neodymium isotopes in sedimentary organic matter. Geochim. Cosmochim. Acta 140, 177–198.
García-Ibáñez, M.I., Pardo, P.C., Carracedo, L.I., Mercier, H., Lherminier, P., Ríos, A.F., Pérez, F.F., 2015. Structure, transports and transformations of the water masses in the Atlantic Subpolar Gyre. Prog. Oceanogr. 135, 18–36.
García-Ibáñez, M.I., Pérez, F.F., Lherminier, P., Zunino, P., Mercier, H., Tréguer, P., 2018. Water mass distributions and transports for the 2014 GEOVIDE cruise in the North Atlantic. Biogeosciences 15, 2075–2090.
Garcia-Solsona, E., Jeandel, C., 2020. Balancing rare earth element distributions in the Northwestern Mediterranean Sea. Chem. Geol. 532, 119372.
Garcia-Solsona, E., Jeandel, Catherine, Labatut, Marie, Lacan, François, Vance, Derek, Chavagnac, Valérie, Pradoux, Catherine, 2014. Rare earth elements and Nd isotopes tracing water mass mixing and particle-seawater interactions in the SE Atlantic. Geochim. Cosmochim. Acta 125, 351–372.
Gourain, A., Planquette, H., Cheize, M., Lemaitre, N., Menzel Barraqueta, J.-L., Shelley, R., Lherminier, P., Sarthou, G., 2019. Inputs and processes affecting the distribution of particulate iron in the North Atlantic along the GEOVIDE (GEOTRACES GA01) section. Biogeosciences 16, 1563–1582.
Greaves, M.J., Statham, P.J., Elderfield, H., 1994. Rare earth element mobilization from marine atmospheric dust into seawater. Mar. Chem. 46, 255–260.
Grenier, M., Garcia-Solsona, E., Lemaitre, N., Trull, T.W., Bouvier, V., Nonnotte, P., van Beek, P., Souhaut, M., Lacan, F., Jeandel, C., 2018. Differentiating Lithogenic Supplies, Water Mass Transport, and Biological Processes On and Off the Kerguelen Plateau Using Rare Earth Element Concentrations and Neodymium Isotopic Compositions. Front. Mar. Sci. 5, 426. https://doi.org/10.3389/fmars.2018.00426.
Grenier, M., Jeandel, C., Lacan, F., Vance, D., Venchiarutti, C., Cros, A., Cravatte, S., 2013. From the subtropics to the central equatorial Pacific Ocean: neodymium isotopic composition and rare earth element concentration variations: Nd Isotopic composition and REE variations. J. Geophys. Res. Oceans 118, 592–618.
Haley, B.A., Klinkhammer, G.P., McManus, J., 2004. Rare earth elements in pore waters of marine sediments. Geochim. Cosmochim. Acta 68, 1265–1279.
Haley, B.A., Klinkhammer, G.P., Mix, A.C., 2005. Revisiting the rare earth elements in foraminiferal tests. Earth Planet. Sci. Lett. 239, 79–97.
Hara, Y., Obata, H., Doi, T., Hongo, Y., Gamo, T., Takeda, S., Tsuda, A., 2009. Rare earth elements in seawater during an iron-induced phytoplankton bloom of the western subarctic Pacific (SEEDS-II). Deep Sea Res Part II Top. Stud. Oceanogr. 56, 2839–2851.
Harkins, W.D., 1917. The evolution of the elements and the stability of complex atoms. I. A new periodic system which shows a relation between the abundance of the elements and the structure of the nuclei of atoms. J. Am. Chem. Soc. 39, 856–879.
Haskin, M.A., Haskin, L.A., 1966. Rare earths in European Shales: a redetermination. Science 154, 507–509.
Hatje, V., Bruland, K.W., Flegal, A.R., 2014. Determination of rare earth elements after pre-concentration using NOBIAS-chelate PA-1®resin: Method development and application in the San Francisco Bay plume. Mar. Chem. 160, 34–41. https://doi.org/10.1016/j.marchem.2014.01.006.
Henderson, G.M., Anderson, R.F., Adkins, J., Andersson, P., Boyle, E.A., Cutter, G., de Baar, H., Eisenhauer, A., Frank, M., Francois, R., Orians, K., Gamo, T., German, C., Jenkins, W., Moffett, J., Jeandel, C., Jickells, T., Krishnaswami, S., Mackey, D., Measures, C.I., Moore, J.K., Oschlies, A., Pollard, R., van der Loeff, M.R., Schlitzer, R., Sharma, M., von Damm, K., Zhang, J., Masque, P., Grp, S.W., 2007. GEOTRACES - an international study of the global marine biogeochemical cycles of trace elements and their isotopes. Chem. Erde-Geochem. 67, 85–131.
Homoky, W.B., Conway, T.M., John, S.G., König, D., Deng, F., Tagliabue, A., Mills, R.A., 2021. Iron colloids dominate sedimentary supply to the ocean interior. Proc. Natl. Acad. Sci. 118, e2016078118.
Jeandel, C., 2016. Overview of the mechanisms that could explain the 'Boundary Exchange' at the land–ocean contact. Philos. Trans. R. Soc. A Math. Phys. Eng. Sci. 374, 20150287.
Jeandel, C., Oelkers, E.H., 2015. The influence of terrigenous particulate material dissolution on ocean chemistry and global element cycles. Chem. Geol. 395, 50–66.
Jeandel, C., Bishop, J.K., Zindler, A., 1995. Exchange of neodymium and its isotopes between seawater and small and large particles in the Sargasso Sea. Geochim. Cosmochim. Acta 59, 535–547.
Jeandel, C., Thouron, D., Fieux, M., 1998. Concentrations and isotopic compositions of neodymium in the eastern Indian Ocean and Indonesian straits. Geochim. Cosmochim. Acta 62, 2597–2607.
Jeandel, C., Arsouze, T., Lacan, F., Téchiné, P., Dutay, J.-C., 2007. Isotopic Nd compositions and concentrations of the lithogenic inputs into the ocean: A compilation, with an emphasis on the margins. Chem. Geol. 239, 156–164.
Jeandel, C., Delattre, H., Grenier, M., Pradoux, C., Lacan, F., 2013. Rare earth element concentrations and Nd isotopes in the Southeast Pacific Ocean. Geochem. Geophys. Geosyst. 14, 328–341.
Jones, K.M., Khatiwala, S.P., Goldstein, S.L., Hemming, S.R., van de Flierdt, T., 2008. Modeling the distribution of Nd isotopes in the oceans using an ocean general circulation model. Earth Planet. Sci. Lett. 272, 610–619.
Keltjens, J.T., Pol, A., Reimann, J., Op den Camp, H.J.M., 2014. PQQ-dependent methanol dehydrogenases: rare-earth elements make a difference. Appl. Microbiol. Biotechnol. 98, 6163–6183.
Khatiwala, S., Tanhua, T., Mikaloff, Fletcher S., Gerber, M., Doney, S.C., Graven, H.D., Gruber, N., McKinley, G.A., Murata, A., Ríos, A.F., Sabine, C.L., 2013. Global Ocean storage of anthropogenic carbon. Biogeosciences 10, 2169–2191.
Kuss, J., Garbe-Schönberg, C.-D., Kremling, K., 2001. Rare earth elements in suspended particulate material of North Atlantic surface waters. Geochim. Cosmochim. Acta 65, 187–199.
Lacan, F., Jeandel, C., 2001. Tracing Papua New Guinea imprint on the central Equatorial Paci¢c Ocean using neodymium isotopic compositions and rare Earth Element patterns. Earth Planet. Sci. Lett. 497–512.
Lacan, F., Jeandel, C., 2001. Tracing Papua New Guinea imprint on the central Equatorial Paci¢c Ocean using neodymium isotopic compositions and Rare Earth Element patterns. Earth Planet. Sc. Lett. 497–512.
Lacan, F., Jeandel, C., 2004a. Neodymium isotopic composition and rare earth element concentrations in the deep and intermediate Nordic Seas: constraints on the Iceland Scotland Overflow Water signature. Geochem. Geophys. Geosyst. 5.
Lacan, François, Jeandel, C., 2004b. Subpolar mode water formation traced by neodymium isotopic composition. Geophys. Res. Lett. 31.
Lacan, F., Jeandel, C., 2005a. Acquisition of the neodymium isotopic composition of the North Atlantic Deep Water: neodymium isotopic composition. Geochem. Geophys. Geosyst. 6, Q12008.
Lacan, F., Jeandel, C., 2005b. Neodymium isotopes as a new tool for quantifying exchange fluxes at the continent–ocean interface. Earth Planet. Sci. Lett. 232, 245–257.
Lagarde, M., Lemaitre, N., Planquette, H., Grenier, M., Belhadj, M., Lherminier, P., Jeandel, C., 2020. Particulate rare earth element behavior in the North Atlantic (GEOVIDE cruise). Biogeosciences 17, 5539–5561.
Lagarde, M., Pham, V.Q., Lemaitre, N., Belhadj, M., Jeandel, C., 2024. Rare earth elements in the North Atlantic, part II: partition coefficients. Chem. Geol.
Lam, P.J., Heller, M.I., Lerner, P.E., Moffett, J.W., Buck, K.N., 2020. Unexpected source and transport of iron from the deep peru margin. ACS Earth Space Chem. 4, 977–992.
Lambelet, M., van de Flierdt, T., Crocket, K., Rehkämper, M., Kreissig, K., Coles, B., Rijkenberg, M.J.A., Gerringa, L.J.A., de Baar, H.J.W., Steinfeldt, R., 2016. Neodymium isotopic composition and concentration in the western North Atlantic

Ocean: results from the GEOTRACES GA02 section. Geochim. Cosmochim. Acta 177, 1–29.
Lawrence, R.M., Shrikumar, A., Le Roy, E., Swift, J.H., Lam, P.J., Cutter, G., Casciotti, K. L., 2022. Water mass analysis of the 2018 US GEOTRACES Pacific Meridional Transect (GP15). Oceanography. https://doi.org/10.1002/essoar.10510438.1.
Le Roy, E., Sanial, V., Charette, M.A., van Beek, P., Lacan, F., Jacquet, S.H.M., Henderson, P.B., Souhaut, M., García-Ibáñez, M.I., Jeandel, C., Pérez, F.F., Sarthou, G., 2018. The 226Ra–Ba relationship in the North Atlantic during GEOTRACES-GA01. Biogeosciences 15, 3027–3048.
Lemaitre, N., Planquette, H., Sarthou, G., Jacquet, S., García-Ibáñez, M.I., Gourain, A., Cheize, M., Monin, L., André, L., Laha, P., Terryn, H., Dehairs, F., 2018. Particulate barium tracing of significant mesopelagic carbon remineralisation in the North Atlantic. Biogeosciences 15, 2289–2307.
Longhurst, A.R., 2010. Ecological Geography of the Sea, 2nd ed. Academic Press, San Diego.
Martin, J.H., Gordon, M., Fitzwater, S.E., 1991. The case for iron. Limnol. Oceanogr. 36, 1793–1802.
Menzel Barraqueta, J.-L., Schlosser, C., Planquette, H., Gourain, A., Cheize, M., Boutorh, J., Shelley, R., Contreira, Pereira L., Gledhill, M., Hopwood, M.J., Lacan, F., Lherminier, P., Sarthou, G., Achterberg, E.P., 2018. Aluminium in the North Atlantic Ocean and the Labrador Sea (GEOTRACES GA01 section): roles of continental inputs and biogenic particle removal. Biogeosciences 15, 5271–5286.
Mercier, H., Lherminier, P., Sarafanov, A., Gaillard, F., Daniault, N., Desbruyères, D., Falina, A., Ferron, B., Gourcuff, C., Huck, T., Thierry, V., 2015. Variability of the meridional overturning circulation at the Greenland–Portugal OVIDE section from 1993 to 2010. Prog. Oceanogr. 132, 250–261. https://doi.org/10.1016/j.pocean.2013.11.001.
Meyer, A.C.S., Grundle, D., Cullen, J.T., 2021. Selective uptake of rare earth elements in marine systems as an indicator of and control on aerobic bacterial methanotrophy. Earth Planet. Sci. Lett. 558, 116756.
Moffett, J.W., 1990. Microbially mediated cerium oxidation in sea water. Nature 345, 421–423.
Moffett, J.W., 1994. The relationship between cerium and manganese oxidation in the marine environment. Limnol. Oceanogr. 39, 1309–1318.
Morel, F.M.M., Price, N.M., 2003. The Biogeochemical Cycles of Trace Metals in the Oceans. Science 300, 944–947.
Nozaki, Y., Alibo, D.S., 2003. Importance of vertical geochemical processes in controlling the oceanic profiles of dissolved rare earth elements in the northeastern Indian Ocean. Earth Planet. Sci. Lett. 205, 155–172.
Ohta, A., Kawabe, I., 2001. REE(III) adsorption onto Mn dioxide (d-MnO2) and Fe oxyhydroxide: Ce(III) oxidation by d-MnO2. Geochim. Cosmochim. Acta 65, 695.
Oka, A., Hasumi, H., Obata, H., Gamo, T., Yamanaka, Y., 2009. Study on vertical profiles of rare earth elements by using an ocean general circulation model: simulation of REEs by OGCM. Glob. Biogeochem. Cycles 23 n/a-n/a.
Osborne, A.H., Haley, B.A., Hathorne, E.C., Plancherel, Y., Frank, M., 2015. Rare earth element distribution in Caribbean seawater: Continental inputs versus lateral transport of distinct REE compositions in subsurface water masses. Mar. Chem. 177, 172–183. https://doi.org/10.1016/j.marchem.2015.03.013.
Pahnke, K., van de Flierdt, T., Jones, K.M., Lambelet, M., Hemming, S.R., Goldstein, S.L., 2012. GEOTRACES intercalibration of neodymium isotopes and rare earth element concentrations in seawater and suspended particles. Part 2: Systematic tests and baseline profiles. Limnology and Oceanography. Methods 10, 252–269. https://doi.org/10.4319/lom.2012.10.252.
Peters, B.D., Jenkins, W.J., Swift, J.H., German, C.R., Moffett, J.W., Cutter, G.A., Brzezinski, M.A., Casciotti, K.L., 2018. Water mass analysis of the 2013 US GEOTRACES eastern Pacific zonal transect (GP16). Mar. Chem. 201, 6–19.
Pham, V.Q., 2020. Traçage de l'empreinte lithogénique en mers de Corail et des Salomon : apport des terres rares et de la composition isotopique du neodyme. Université de Toulouse III – Paul Sabatier.
Pham, V.Q., Grenier, M., Cravatte, S., Michael, S., Jacquet, S., Belhadj, M., Nachez, Y., Germineaud, C., Jeandel, C., 2019. Dissolved rare earth elements distribution in the Solomon Sea. Chem. Geol. 524, 11–36.
Quinn, K.A., Byrne, R.H., Schijf, J., 2006. Sorption of yttrium and rare earth elements by amorphous ferric hydroxide: Influence of solution complexation with carbonate. Geochimica et Cosmochimica Acta 70, 4151–4165. https://doi.org/10.1016/j.gca.2006.06.014.
Rousseau, T.C.C., Sonke, J.E., Chmeleff, J., van Beek, P., Souhaut, M., Boaventura, G., Seyler, P., Jeandel, C., 2015. Rapid neodymium release to marine waters from lithogenic sediments in the Amazon estuary. Nat. Commun. 6, 7592.
Roy-Barman, M., Foliot, L., Douville, E., Leblond, N., Gazeau, F., Bressac, M., Wagener, T., Ridame, C., Desboeufs, K., Guieu, C., 2021. Contrasted release of insoluble elements (Fe, Al, rare earth elements, Th, Pa) after dust deposition in seawater: a tank experiment approach. Biogeosciences 18, 2663–2678.
Sarthou, G., Lherminier, P., Achterberg, E.P., Alonso-Pérez, F., Bucciarelli, E., Boutorh, J., Bouvier, V., Boyle, E.A., Branellec, P., Carracedo, L.I., Casacuberta, N., Castrillejo, M., Cheize, M., Contreira, Pereira L., Cossa, D., Daniault, N., De Saint-Léger, E., Dehairs, F., Deng, F., Desprez de Gésincourt, F., Devesa, J., Foliot, L., Fonseca-Batista, D., Gallinari, M., García-Ibáñez, M.I., Gourain, A., Grossteffan, E., Hamon, M., Heimbürger, L.E., Henderson, G.M., Jeandel, C., Kermabon, C., Lacan, F., Le Bot, P., Le Goff, M., Le Roy, E., Lefèbvre, A., Leizour, S., Lemaitre, N., Masqué, P., Ménage, O., Menzel Barraqueta, J.-L., Mercier, H., Perault, F., Pérez, F. F., Planquette, H.F., Planchon, F., Roukaerts, A., Sanial, V., Sauzède, R., Schmechtig, C., Shelley, R.U., Stewart, G., Sutton, J.N., Tang, Y., Tisnérat-Laborde, N., Tonnard, M., Tréguer, P., van Beek, P., Zurbrick, C.M., Zunino, P., 2018. Introduction to the French GEOTRACES North Atlantic Transect (GA01): GEOVIDE cruise. Biogeosciences 15, 7097–7109.
Schijf, J., Christenson, E.A., Byrne, R.H., 2015. YREE scavenging in seawater: A new look at an old model. Mar. Chem 177, 460–471. https://doi.org/10.1016/j.marchem.2015.06.01.
Schlitzer, R., 2023. Ocean Data View. https://odv.awi.de.
Shiller, A.M., 2021. Dissolved rare earth element (REE) concentrations from the GEOTRACES North Atlantic Transect (Section GA03) collected on the R/V Knorr cruises KN199–04, KN199–05, and KN204–01 during 2010 and 2011. (Version 2) Version Date 2021-07-28.
Shiller, A.M., Chan, E.W., Joung, D.J., Redmond, M.C., Kessler, J.D., 2017. Light rare earth element depletion during Deepwater Horizon blowout methanotrophy. Sci. Rep. 7, 10389.
Sholkovitz, E.R., 1992. Chemical evolution of rare earth elements: fractionation between colloidal and solution phases of filtered river water. Earth Planet. Sci. Lett. 114, 77–84.
Sholkovitz, E.R., Landing, W.M., Lewis, B.L., 1994. Ocean particle chemistry: the fractionation of rare earth elements between suspended particles and seawater. Geochim. Cosmochim. Acta 58, 1567–1579.
Sholkovitz, E.R., Elderfield, H., Szymczak, R., Casey, K., 1999. Island weathering: river sources of rare earth elements to the Western Pacific Ocean. Mar. Chem. 68, 39–57.
Siddall, M., Khatiwala, S., van de Flierdt, T., Jones, K., Goldstein, S.L., Hemming, S., Anderson, R.F., 2008. Towards explaining the Nd paradox using reversible scavenging in an ocean general circulation model. Earth Planet. Sci. Lett. 274, 448–461.
Stichel, T., Frank, M., Rickli, J., Haley, B.A., 2012. The hafnium and neodymium isotope composition of seawater in the Atlantic sector of the Southern Ocean. Earth Planet. Sci. Lett. 317–318, 282–294. https://doi.org/10.1016/j.epsl.2011.11.025.
Sutorius, M., Mori, C., Greskowiak, J., Boettcher, L., Bunse, C., Dittmar, T., Dlugosch, L., Hintz, N.H., Simon, M., Striebel, M., Pahnke, K., 2022. Rare earth element behaviour in seawater under the influence of organic matter cycling during a phytoplankton spring bloom – A mesocosm study. Front. Mar. Sci. 9, 895723.
Tachikawa, K., Jeandel, C., Roy-Barman, M., 1999. A new approach to the Nd residence time in the ocean: the role of atmospheric inputs. Earth Planet. Sci. Lett. 170, 433–446.
Tachikawa, K., Athias, V., Jeandel, C., 2003. Neodymium budget in the modern ocean and paleo-oceanographic implications. J. Geophys. Res. Oceans 108.
Taylor, S.R., McLennan, S.M., 1985. The Continental Crust: Its Composition and Evolution. Blackwell Scientific, Boston, Mass.
Thierry, V., de Boisséson, E., Mercier, H., 2008. Interannual variability of the Subpolar Mode Water properties over the Reykjanes Ridge during 1990–2006. J. Geophys. Res. 113, C04016. https://doi.org/10.1029/2007JC004443.
Tomczak, M., 1981. A multi-parameter extension of temperature/salinity diagram techniques for the analysis of non-isopycnal mixing. Prog. Oceanogr. 10, 147–171.
Tomczak, M., 1999. Some historical, theoretical and applied aspects of quantitative water mass analysis. J. Mar. Res. 57, 275–303.
Tomczak, M., Large, D.G.B., 1989. Optimum multiparameter analysis of mixing in the thermocline of the eastern Indian Ocean. J. Geophys. Res. 94, 16141.
Tonnard, M., 2018. Etude du cycle biogéochimique du fer: distribution et spéciation dans l'Océan Atlantique Nord (GA01) et l'Océan Austral (GIpr05) (GEOTRACES), p. 412.
Tonnard, M., Planquette, H., Bowie, A., van der Merwe, P., Gallinari, M., Desprez de Gésincourt, F., Germain, Y., Gourain, A., Benetti, M., Reverdin, G., Tréguer, P., Boutorh, J., Cheize, M., Menzel Barraqueta, J.-L., Pereira-Contreira, L., Shelley, R., Lherminier, P., Sarthou, G., 2018. Dissolved iron in the North Atlantic Ocean and Labrador Sea along the GEOVIDE section (GEOTRACES section GA01). Biogeosci. Discuss. 1–53.
van de Flierdt, T., Griffiths, A.M., Lambelet, M., Little, S.H., Stichel, T., Wilson, D.J., 2016. Neodymium in the oceans: a global database, a regional comparison and implications for palaeoceanographic research. Phil. Trans. R. Soc. A. 374, 20150293. https://doi.org/10.1098/rsta.2015.0293.
Wilson, D.J., Piotrowski, A.M., Galy, A., McCave, I.N., 2012. A boundary exchange influence on deglacial neodymium isotope records from the deep western Indian Ocean. Earth Planet. Sci. Lett. 341–344, 35–47.
Xu, A., Hathorne, E., Laukert, G., Frank, M., 2023. Overlooked riverine contributions of dissolved neodymium and hafnium to the Amazon estuary and oceans. Nat. Commun. 14, 4156.
Yeghicheyan, D., Aubert, D., Coz, M.B.-L., Chmeleff, J., Delpoux, S., Djouraev, I., Granier, G., Lacan, F., Piro, J.-L., Rousseau, T., Cloquet, C., Marquet, A., Menniti, C., Pradoux, C., Freydier, R., Silva-Filho, E.V.da, Suchorski, K., 2019. A New Interlaboratory Characterisation of Silicon, Rare Earth Elements and Twenty-Two Other Trace Element Concentrations in the Natural River Water Certified Reference Material SLRS-6 (NRC-CNRC). Geostand. Geoanalytical Res. 43, 475–496. https://doi.org/10.1111/ggr.12268.
Zhang, L., Algeo, T.J., Cao, L., Zhao, L., Chen, Z.-Q., Li, Z., 2016. Diagenetic uptake of rare earth elements by conodont apatite. Palaeogeogr. Palaeoclimatol. Palaeoecol. 458, 176–197.
Zhang, Y., Lacan, F., Jeandel, C., 2008. Dissolved rare earth elements tracing lithogenic inputs over the Kerguelen Plateau (Southern Ocean). Deep Sea Research Part II. Top. Stud. Oceanogr. 55, 638–652. https://doi.org/10.1016/j.dsr2.2007.12.029.
Zheng, X.-Y., Plancherel, Y., Saito, M.A., Scott, P.M., Henderson, G.M., 2016. Rare earth elements (REEs) in the tropical South Atlantic and quantitative deconvolution of their non-conservative behavior. Geochim. Cosmochim. Acta 177, 217–237.
Zunino, P., Lherminier, P., Mercier, H., Daniault, N., García-Ibáñez, M.I., Pérez, F.F., 2017. The GEOVIDE cruise in May–June 2014 reveals an intense Meridional Overturning Circulation over a cold and fresh subpolar North Atlantic. Biogeosciences 14, 5323–5342. https://doi.org/10.5194/bg-14-5323-2017.